Germinal center B cells recognize antigen through a specialized immune synapse architecture

Carla R. Nowosad[1], Katelyn M. Spillane[1,2] & Pavel Tolar[1,2]

[1] Laboratory of Activation of Immune Receptors
Francis Crick Institute
Mill Hill Laboratory
London, UK

[2] Division of Immunology and Inflammation
Department of Medicine
Imperial College London
London, UK

Correspondence should be addressed to P.T. (pavel.tolar@crick.ac.uk).

Abstract

B cell activation is regulated by B cell antigen receptor (BCR) signaling and antigen internalization in immune synapses. Using large-scale imaging across B cell subsets, we show that in contrast to naive and memory B cells, which gathered antigen towards the synapse center before internalization, germinal center (GC) B cells extracted antigen by a distinct pathway using small peripheral clusters. Both naive and GC B cell synapses required proximal BCR signaling, but GC cells signaled less through the protein kinase C-β (PKC-β)–NF-κB pathway and produced stronger tugging forces on the BCR, thereby more stringently regulating antigen binding. Consequently, GC B cells extracted antigen with better affinity discrimination than naive B cells, suggesting that specialized biomechanical patterns in B cell synapses regulate T-cell dependent selection of high-affinity B cells in GCs.

Introduction

Antibody responses are triggered when naive B cells bind antigen on the surfaces of antigen-presenting cells (APCs) such as subcapsular macrophages[1-3] and dendritic cells[4,5]. This initiates B cell antigen receptor (BCR) signaling and the formation of an immune synapse. The dynamics and structure of naive B cell synapses resemble those of other lymphocytes[6], and feature signaling-induced cytoskeletal rearrangements[7-10] that lead to initial extension of lamellipodia and cell spreading[7,11], followed by antigen clustering and transport towards the center of the synapse[12]. Unlike other lymphocytes, however, naive B cells quickly contract the synapse and extract the antigen for endocytosis[10], ultimately driving B cell antigen presentation to helper T cells.

Naive B cells that receive T cell help can enter into the germinal center (GC), which is particularly important for affinity maturation of antibodies and the generation of the memory B cell repertoire[13]. GC B cells are highly motile, make large lamellipodial protrusions, and frequently form contacts with follicular dendritic cells (FDCs) that present antigen in the light zone of the GC[14-16]. GC B cells containing somatic mutations that improve affinity for antigen acquire more antigen from FDCs than lower affinity GC B cells do, resulting in a selective advantage during T cell-dependent selection and subsequent proliferation in the GC dark zone[17,18]. This selection requires NF-κB activation, presumably induced by T cell-derived CD40 signaling[19,20]. Although some light zone GC B cells also show signs of BCR signaling[17,21], evidence of general transcriptional[22] and post-translational[23] silencing of BCR signaling in GC B cells exists, which together with the requirement for the T cell help, suggests that BCR signaling is not sufficient for GC B cell selection. However, despite the importance of GC B cell antigen acquisition from synapses with FDCs, GC B cell synapse formation and its contribution to affinity-dependent antigen internalization have not been investigated.

Here we developed an *ex vivo* large-scale imaging approach to quantify synaptic organization, signaling and antigen extraction in thousands of primary B cells. We identified GC B cells as a subset with unique synaptic architecture that was characterized by antigen localization in small clusters at the synapse periphery. We show that recognition of high-affinity membrane antigen by GC B cells triggered strong proximal BCR signaling, but poor signal propagation through protein kinase C-β (PKC-β) to the activation of NF-κB. Proximal BCR signaling was required for antigen extraction, which in GC B cells occured through a phosphoinositide-3-OH kinase (PI(3)K)-independent pathway. We also show that GC B cells

used strong myosin II contractility and high pulling forces on the BCR to directly regulate BCR binding to antigen. Accordingly, the GC synapse was associated with stringent affinity discrimination during antigen extraction. These results indicate that altered BCR signaling and cytoskeletal organization in GC B cells promote affinity-dependent antigen acquisition. However, BCR signaling in GC B cells is insufficient to induce full cell activation, which instead requires signals provided by T cells.

Results

Subset-specific differences in B cell synapses

To obtain a global view of the variations in synaptic architecture in B cells, we developed a large-scale imaging approach (**Supplementary Fig. 1a**). Total splenic B cells were incubated with antigen (anti-Igκ) presented on planar lipid bilayers (PLBs), fixed and stained for surface markers. The samples were imaged by a high magnification multi-color microscope system in 3D, collecting up to a thousand fields of view per imaging chamber. Images were processed by a high-throughput workflow using per-pixel corrections for background, flatfield and spectral bleed-through. Individual B cells were detected based on surface staining by combining an automated 3D segmentation algorithm with semi-automatic quality control to exclude dead cells, debris and artifacts (**Supplementary Fig. 1b,c**). Dotplot displays of surface marker fluorescence intensities allowed identification of splenic B cell subsets with results consistent with flow cytometry (**Fig. 1a,b**). Applying gating to analyzed images based on surface marker expression showed that although the mean intensity of antigen accumulated in synapses was similar amongst all B cell subsets, mature follicular B cells were most efficient in contracting synapses and centralizing the antigen into compact central supramolecular activating clusters (cSMACs, **Fig. 1c**). In contrast, centralization of antigen was lowest in transitional T1 B cells and intermediate in T2-3 transitional B cells, although in both B cell subsets, a substantial fraction of the cells still formed synapses with a cSMAC. Marginal zone B cells formed spread synapses with efficient centralization of antigen into large cSMACs. Thus, all naive B cell subsets centralized antigen in immune synapses, although to varying degrees.

GC B cells exhibit unique synaptic architecture

To analyze synaptic architecture in antigen-experienced B cells, we imaged synapses of splenic B cells from mice immunized with sheep red blood cells (SRBCs). We found that B cells forming synapses with low antigen centralization were highly enriched in the Fas-positive, CD38-negative GC B cell gate (**Fig. 2a**). Gating on all GC B cells revealed that they were larger than naive B cells and had a number of lamellipodia-like protrusions (**Fig. 2b**), as observed previously *in vivo*[14]. Some GC B cells formed small synapses through contacts of cell protrusions with the PLB, but most formed large synapses that contained antigen in small peripheral clusters (**Fig. 2b**). Quantitative analysis showed that GC B cell synapses contained less antigen than naive B cell synapses did (**Fig. 2c**). Furthermore, GC B cells predominantly distributed the antigen into peripheral supramolecular activating clusters (pSMACs), with a

small fraction of cells accumulating antigen into small cSMACs. This synaptic architecture was also detected in GC B cells enriched by depletion of IgD-expressing naive B cells and was associated with distinct patterns of F-actin and microtubule localization (**Fig. 2d, Supplementary Fig. 2**). Compared to naive B cell synapses, which contained F-actin in peripheral lamellipodia and in spots over the cSMAC, GC B cell synapses contained F-actin in structures closely associated with the peripheral antigen clusters (**Fig. 2d**). Naive B cell synapses contained individual microtubules crossing the synapse in close proximity to the plasma membrane. In contrast, most GC B cells did not polarize microtubules to the synapse, although a minority of GC B cells translocated their microtubule organizing centers to the center of the synapse (**Supplementary Fig. 2**). Isotype switching did not have a noticeable effect on the synapses, as IgM-expressing and IgG1-expressing GC B cells had similar synaptic arrangements (**Fig. 2e**). Likewise, IgG1-expressing, Fas^{-}, $CD38^{+}$ memory B cells formed cSMACs resembling those in naive follicular B cells.

We used live cell imaging of the pre-enriched GC B cells to determine the cellular dynamics underlying their unusual synaptic architecture. The phenotype of the cells was verified by staining for GC markers *in situ* after the time lapses were acquired. Live cell imaging showed that GC cells initially spread and form antigen clusters similarly to follicular B cells (**Fig. 3a**, **Supplementary movie 1**). However, while in naive B cell spreading was followed by rapid growth of the antigen clusters, their centripetal movement and fusion into the cSMAC, in GC B cells the antigen clusters grew slower and moved dynamically both inward and outward, sometimes in a pulsating manner, before they were eventually pushed outward to the synapse periphery. Quantification confirmed that antigen cluster growth was slower in GC B cells in the first two minutes of synapse formation (**Fig. 3b,c**). Although the antigen clusters in GC synapses occasionally fused with each other, many remained isolated and underwent dynamic growth and reduction in their antigen content (**Fig. 3b**), with some clusters appearing only transiently, particularly in the center of the synapse (**Supplementary movie 1**). Thus, differentiation of B cells into GC cells is accompanied by cytoskeletal changes that result in fundamentally different dynamics and organization of the immune synapse.

Signaling in synapses of GC B cells

To compare BCR signaling induced by antigens in naive and GC B cells, we measured phosphorylation of BCR signaling components by intracellular staining. When stimulated by soluble antigen, induced phosphorylation of Syk and BLNK was less in GC B cells than in naive B cells, whereas basal phosphorylation of SHIP1 was higher in GC B cells than in

naive B cells and decreased after antigen stimulation (**Supplementary Fig. 3a**), as reported previously[23]. To analyze activation by membrane-presented antigen, we imaged phosphorylated components of BCR signaling pathways in B cells interacting with antigen on plasma membrane sheets (PMSs). PMSs are flexible membrane substrates that support B cell synapse formation, signaling and antigen internalization[10], but cover the imaging chambers sparsely, allowing gating on B cells that either interacted with antigen on the PMSs or remained unstimulated outside of the PMSs (**Fig. 4a**). Control experiments showed that staining with all phospho-specific antibodies was higher in B cells on the PMSs than in B cells outside of PMSs and was sensitive to inhibition of upstream signaling pathways with pharmacological inhibitors (**Supplementary Fig. 3b**). In both naive and GC B cells, image analysis showed colocalization of phosphorylated Syk, BLNK, Jnk and SHIP with antigen clusters in the periphery of synapses, while phosphorylated Erk and Akt were localized throughout the cells (**Fig. 4b** and **Supplementary Fig. 4**). In naive B cells, colocalization of the phosphorylated Syk, BLNK, Jnk and SHIP with antigen decreased on antigen clusters extracted from the synapse. In GC B cells, however, these phosphorylated signaling proteins still associated with the majority of antigen clusters extracted from the synapse. Quantification showed that the mean intensity of phosphorylation in all pathways investigated was higher in GC B cells than in naive B cells (**Fig. 4a,c**). In addition, live cell imaging showed that GC B cells responded to membrane antigen with intracellular calcium fluxes that were similar or slightly higher than in naive B cells (**Fig. 4d**). Consequently, in contrast to stimulation with soluble antigen, GC B cells respond efficiently to membrane-presented antigens and their proximal signaling is not terminated by antigen extraction.

However, unstimulated and stimulated GC B cells stained lower than naive cells with antibodies recognizing the phosphorylated, catalytically competent conventional PKC-α and PKC-β (**Fig. 5a**). Similar results were found using antibodies specific for phosphorylated and total PKC-β, the major conventional PKC in B cells (**Supplementary Fig. 5a,b**). In contrast to naive B cells, PKC-β was not efficiently recruited to the immune synapse in GC B cells (**Fig. 5b** and **Supplementary Fig. 5a,b**) and was poorly translocated to the plasma membrane after treatment with the phorbol ester PMA and the calcium ionophore ionomycin (**Fig. 5c**). These differences were specific for PKC-β as the novel PKCδ was present at higher levels in GC B cells (**Fig. 5d**) and efficiently translocated to the synapse and to the membrane in response to antigen and PMA plus ionomycin, respectively (**Fig. 5e,f**). Inhibition of PKC-β led to a slight reduction of antigen centralization in synapses of naive B cells, but these

synapses did not resemble the pattern observed in GC B cells (**Supplementary Fig. 5c**), suggesting that reduction of PKC-β activity in GC B cells is not a critical determinant of their synaptic architecture. In B cells, PKC-β has a reported role in the activation of the NF-κB pathway downstream of the BCR[24]. Correspondingly, GC B cells translocated NF-κB component p50 into the nucleus less efficiently than naive cells did in response to antigen, but were fully competent in nuclear translocation of p50 induced via CD40, which is not PKC-β dependent (**Fig. 5g).** Thus, these results indicate that while GC B cells trigger BCR signaling efficiently, signal propagation through PKC-β to NF-κB is reduced compared to naive B cells.

Antigen internalization by GC B cells

To analyze antigen internalization from synapses of naive and GC B cells, we first measured activation of myosin contractility, which is important for antigen extraction in naive B cells. Staining for myosin II activated by phosphorylation of the myosin light chain (MLC) was higher in GC B cells than in naive B cells (**Fig. 4c**). Furthermore, whereas the phosphorylated MLC was localized in spots above the cSMAC in naive B cells, in GC B cells it was localized in the periphery of the synapse, in close association with antigen clusters (**Supplementary Fig. 4**). Quantification of antigen extraction from immune synapses showed that GC and naive B cells extracted similar amounts of antigen, although GC B cells extracted the antigen in smaller, more numerous clusters (**Fig. 6a,b**). To quantify the amount of extracted antigen that reached degradative endosomal compartments for processing, we conjugated the antigen to a degradation sensor composed of a double-stranded DNA oligomer with an Atto647N fluorophore and a dark quencher in close proximity. Upon enzymatic cleavage of this sensor in endosomes, the Atto647N fluorescence is unquenched (**Fig. 6c,d**). We observed degradation of most of the extracted antigen in naive B cells, in contrast to GC B cells, where degradation was less efficient. To test whether the difference in antigen degradation could be due to a delay in antigen internalization by GC B cells relative to naive B cells, we stained the cells with antibodies against the anti-Igκ antigen to identify antigen that remained on the cell surface. We observed that the majority of the antigen extracted by naive B cells was inaccessible to the staining, indicating that it had been internalized, while a large fraction of the antigen extracted by GC B cells was stained on the sides of the cells (**Fig. 6e,f**). Thus, naive B cells endocytose antigen directly in synapses, whereas GC B cells first extract antigen from the antigen-presenting surface and then transport it toward the opposite pole of the cell before endocytosing it. This mechanism of

antigen endocytosis was specific to membrane-presented antigens, because internalization and degradation of soluble antigens was comparable between naive and GC B cells (**Supplementary Fig. 6**).

To understand how antigen extraction is regulated in naive and GC B cells, we treated the cells with inhibitors of BCR signaling and contractility. Inhibition of Src kinases using PP2 or Bosutinib, the Syk kinase using Bay61-3606 or PRT062607, or myosin II using blebbistatin reduced antigen extraction in both naive and GC B cells (**Fig. 6g**). This finding suggests that similarly to naive B cells, GC B cells require BCR signaling and myosin contractility for antigen extraction from membrane substrates. Inhibition of PKC-β had no effect on antigen extraction in either cell type (**Supplementary Fig. 5d**). In contrast, inhibition by the broad-spectrum PI(3)K inhibitor LY294002, or the class I-specific PI(3)K inhibitor GDI-0941 abolished antigen extraction in naive B cells, but had only a modest effect in GC B cells (**Fig. 6g**), suggesting that GC B cells extract the antigen by a molecularly distinct mechanism.

Mechanical force generation in GC B cells

The small size of antigen clusters and high levels of myosin activity in GC B cell synapses suggest that GC B cells may be mechanically more active and actively use contractility to regulate BCR binding to antigen. To compare the magnitude and dynamics of pulling forces applied by naive and GC cells on the BCR-antigen bond, we conjugated anti-Igκ to DNA-based force sensors (**Supplementary Fig. 7a**). These force sensors contain a central DNA hairpin that unwinds under pulling forces exerted on the antigen, which displaces an Atto647N dye from a dark quencher at the base of the hairpin, leading to an increase in Atto647N fluorescence over the force-insensitive fluorescence of an Atto550 label. The sensors were designed with hairpins that open at 7, 9, or 14 pN[25], including a control that lacks the hairpin and cannot be opened by force. To compare the dynamics of tensile forces in B cell synapses, we attached the antigen-containing force sensors to PLBs, which offer little resistance to lateral movement, but strongly resist tensile displacement, preventing antigen extraction[10]. Time-lapse imaging with the 9 pN sensor showed only rare and transient sensor opening in naive B cell synapses (**Fig. 7a**, **Supplementary movie 2**). However, GC B cells dynamically opened this sensor in the majority of the synaptic clusters. Tracking of antigen clusters showed that the GC B cells applied forces in short repetitive bursts lasting five to ten seconds and that the frequency of the bursts increased with time. Some bursts of force coincided with a decrease in cluster fluorescence in the Atto550 channel (**Fig. 7b**),

suggesting concomitant reduction in antigen binding. In contrast, in naive B cell synapses, antigen clusters grew steadily in size and fused into the cSMAC before the onset of force application. Quantification of the Atto647N/Atto550 fluorescence ratio for each of the sensors showed that naive B cells partially opened the 7 pN sensor, but could not open the 9 or 14 pN sensors (**Fig. 7c**). In contrast, GC B cells opened the 7 pN sensor significantly more efficiently than naive B cells and could also partially open the 9 and 14 pN sensors. The opening of the sensors was specific to force application as none of the cells could open the control sensor lacking the force-sensitive hairpin (**Fig. 7c**). Thus, GC B cells apply stronger and more persistent tensile forces on the BCR than naive B cells do.

To determine the effects of mechanical forces on antigen binding in immune synapses of naive and GC B cells, we measured the mean anti-Igκ antigen intensity over time in synapses of control or myosin II-inhibited cells interacting with PLBs, from which antigens are not extracted (**Fig. 7c**, **Supplementary Fig. 7b**). In naive B cells, inhibition of myosin II only modestly increased antigen binding. However, consistent with the strong forces generated on antigen clusters, myosin II inhibition significantly improved binding of antigen in GC B cells, suggesting that GC B cells use myosin II contractility to negatively regulate antigen binding through mechanical forces.

We have previously shown that the strength and timing of mechanical forces in immune synapses can promote affinity discrimination[26]. To measure affinity discrimination during antigen extraction in naive and GC B cells, we transferred naive B1-8 B cells specific for the low-affinity 4-hydroxy-3-nitrophenylacetyl (NP) and the high-affinity 4-hydroxy-3-iodo-5-nitrophenylacetyl (NIP) haptens into wild-type C57BL/6 mice, before immunization with NIP-conjugated SRBC. Control staining confirmed that the B1-8 B cells that differentiated into GC B cells after immunization bound soluble NP_{15} and NIP_{15} multivalent antigens with similar avidity (**Supplementary Fig 8a**). In addition, both the B1-8 naive and GC B cells bound soluble monovalent NP with similarly lower affinity than soluble monovalent NIP (**Supplementary Fig 8b**). Quantification of BLNK phosphorylation in synapses with NP_{15} and NIP_{15} antigens on PMSs showed that naive and GC B1-8 B cells phosphorylated BLNK similarly in response to the two antigens (**Fig. 8a**). However, in contrast to experiments with the high affinity anti-Igκ antigen, B1-8 GC B cells phosphorylated BLNK less than naive B1-8 B cells did. Both B1-8 naive and B1-8 GC B cells extracted more NIP_{15} antigen than NP_{15} antigen (**Fig. 8b**), but the ratio of extracted NIP_{15} to NP_{15} was significantly larger in B1-8 GC B cells than in B1-8 naive B cells (**Fig. 8c**), indicating that GC B cells achieve more

stringent affinity discrimination during extraction of antigen from immune synapses than naive B cells do.

Discussion

Previous studies of naive follicular B cells established that synapse formation is characterized by gathering of antigen clusters into the center of the synapse[7,27]. Through large-scale quantitative analysis, we show here that all naive and memory B cell subsets formed such canonical synapses, with a developmental increase in antigen centralization from transitional to follicular B cells. Cytoskeleton-dependent antigen centralization has been associated with regulation of BCR signaling and autoimmunity[28-30], suggesting that the degree of antigen centralization could control B cell activation in a subset-specific manner.

Unlike naive and memory B cells, however, GC B cells formed synapses with small antigen clusters present at the periphery of the synapse. Although synapses with incomplete antigen centralization have been observed under some conditions in T cells[31,32], the synapses of GC B cells were different in that an active centrifugal flow pushed the antigen clusters to the edges of the synapse, from where the clusters were transferred from the antigen-presenting surface to the B cell. The architecture of GC B cell synapses was not associated with BCR class switching or qualitatively different proximal BCR signaling. Instead, our data suggest that the architecture of GC synapses is regulated by the effects of the GC differentiation program on the B cell cytoskeleton. The synapses of GC B cells lacked microtubule polarization, but contained F-actin structures colocalized with antigen and were associated with high levels of myosin II contractility. The retraction of GC B cells away from the membrane antigen is reminiscent of contact-mediated repulsion and may be important for GC B cells to limit their contact time with individual FDCs in favor of continuous sampling of the GC light zone for antigen[33]. Future studies of interactions of GC B cells with live FDCs will be needed to investigate this possibility.

Although BCR signaling in response to soluble antigens is dampened in GC B cells[23], our imaging shows that GC B cells activate BCR signaling efficiently in response to membrane-presented antigens. A fraction of light zone GC B cells undergoing selection show activation of the Nur77 reporter, suggesting that BCR signaling is activated in these cells *in vivo*[21]. It is possible that membrane-presented antigens provide mechanical stimuli that promote BCR signaling, as has been observed in follicular B cells[34]. Alternatively, immune synapses may exclude inhibitors of BCR triggering[6]. In any case, we show here that BCR signaling is necessary for membrane antigen extraction by GC B cells, and is therefore expected to play an important role in antigen presentation and eventually in T-cell dependent GC B cell selection.

Although BCR proximal signaling was efficient in GC B cells, recruitment of PKC-β to the synapse was reduced and antigen-induced nuclear translocation of the p50 component of NF-κB was inefficient. The exact reason for low PKC-β signaling will require further study. According to public databases, PKC-β mRNA levels are reduced in GC B cells (www.immgen.org) and our data show lower amounts of total and phosphorylated PKC-β protein in GC B cells and poor membrane recruitment even when bypassing BCR signaling by PMA and ionomycin, suggesting that silencing of the pathway at the level of PKC-β contributes to this effect. Since NF-κB activity has been implicated in induction of c-Myc and proliferation of positively selected GC B cells[20,35], these data are consistent with the notion that BCR-derived signals are not sufficient to drive GC B cell selection, which proceeds only after CD40 signaling induced by follicular helper T cells[13,36].

The structure and dynamics of GC B cell synapses imply that they are specialized for force-mediated antigen extraction and stringent affinity discrimination. Using new nanosensors for measurement of cellular forces[38-40], we show that GC B cells apply tugging forces on the antigen that are stronger and more persistent than those applied by naive B cells. The stronger forces applied in GC B cell synapses regulated BCR binding to the antigen, likely by increasing the dissociation rate of the bond. The increased bond dissociation rate, together with the lower bond association rate due to lower surface BCR density in GC B cells, is expected to improve affinity discrimination and extend it into the higher affinity range. Our data indeed show that GC B cells achieved more stringent affinity discrimination than naive B cells.

In addition to higher forces, GC B cells extracted antigen by a distinct, PI(3)K-independent mechanism. Unlike naive cells, which pinch off the antigen-presenting membranes by synaptic clathrin-coated pits[10], GC B cells likely need to physically separate the antigen away from the FDCs before endocytosis. This direct antigen extraction could serve to compare BCR affinity to the affinity of the antibodies that bind the antigen via immune complexes to the FDCs, and can could therefore create a selection pressure on the BCR to outcompete existing antibody specificities[37]. In addition, the extracted antigen on GC B cell surfaces could be acquired by another GC B cell recognizing a different epitope with better affinity. All of these mechanisms could improve the stringency of affinity-based selection within the GC. In conclusion, B cells can mechanically regulate antigen affinity discrimination by generating distinct cytoskeletal patterns in immune synapses[26]. Determining the molecular

basis of these biomechanical differences between naive and GC cells will be important to better understand B cell clonal selection during antibody responses.

Acknowledgements

This work was supported by the European Research Council Consolidator Grant number 648228 (K.M.S. and P.T.), and by the Francis Crick Institute, which receives its core funding from Cancer Research UK, the UK Medical Research Council, and the Wellcome Trust (C.R.N., K.M.S. and P.T.). In addition, P. T. is supported by the EMBO Young Investigator Programme.

Author contributions

C.R.N. performed immunizations, cell transfers, flow cytometry, large-scale and live cell imaging, and commented on the manuscript. K.M.S. designed degradation sensors, force sensors and monovalent antigens, performed force measurements and live cell imaging, analyzed data and commented on the manuscript. P.T. supervised the work, conceived and carried out the large scale imaging data analysis, and wrote the manuscript.

References

1. Carrasco, Y. R. & Batista, F. D. B cells acquire particulate antigen in a macrophage-rich area at the boundary between the follicle and the subcapsular sinus of the lymph node. *Immunity* **27,** 160–171 (2007).
2. Phan, T. G., Grigorova, I., Okada, T. & Cyster, J. G. Subcapsular encounter and complement-dependent transport of immune complexes by lymph node B cells. *Nat. Immunol.* **8,** 992–1000 (2007).
3. Junt, T. *et al.* Subcapsular sinus macrophages in lymph nodes clear lymph-borne viruses and present them to antiviral B cells. *Nature* **450,** 110-114 (2007).
4. Gonzalez, S. F. *et al.* Capture of influenza by medullary dendritic cells via SIGN-R1 is essential for humoral immunity in draining lymph nodes. *Nat. Immunol.* **11,** 427–434 (2010).
5. Qi, H., Egen, J. G., Huang, A. Y. C. & Germain, R. N. Extrafollicular activation of lymph node B cells by antigen-bearing dendritic cells. *Science* **312,** 1672–1676 (2006).
6. Batista, F. D., Iber, D. & Neuberger, M. S. B cells acquire antigen from target cells after synapse formation. *Nature* **411,** 489–494 (2001).
7. Fleire, S. J. *et al.* B cell ligand discrimination through a spreading and contraction response. *Science* **312,** 738–741 (2006).
8. Schnyder, T. *et al.* B cell receptor-mediated antigen gathering requires ubiquitin ligase Cbl and adaptors Grb2 and Dok-3 to recruit dynein to the signaling microcluster. *Immunity* **34,** 905–918 (2011).
9. Yuseff, M.-I. I. *et al.* Polarized secretion of lysosomes at the B cell synapse couples antigen extraction to processing and presentation. *Immunity* **35,** 361–374 (2011).
10. Natkanski, E. *et al.* B cells use mechanical energy to discriminate antigen affinities. *Science* **340,** 1587–1590 (2013).
11. Weber, M. *et al.* Phospholipase C-γ2 and Vav cooperate within signaling microclusters to propagate B cell spreading in response to membrane-bound antigen. *J. Exp. Med.* **205,** 853–868 (2008).
12. Liu, W., Meckel, T., Tolar, P., Sohn, H. W. & Pierce, S. K. Antigen affinity discrimination is an intrinsic function of the B cell receptor. *J. Exp. Med.* **207,** 1095–1111 (2010).
13. Victora, G. D. & Nussenzweig, M. C. Germinal centers. *Annu. Rev. Immunol.* **30,** 429–457 (2012).

14. Allen, C. D. C., Okada, T., Tang, H. L. & Cyster, J. G. Imaging of germinal center selection events during affinity maturation. *Science* **315,** 528–531 (2007).
15. Hauser, A. E. *et al.* Definition of germinal-center B cell migration in vivo reveals predominant intrazonal circulation patterns. *Immunity* **26,** 655–667 (2007).
16. Schwickert, T. A. *et al.* In vivo imaging of germinal centres reveals a dynamic open structure. *Nature* **446,** 83–87 (2007).
17. Victora, G. D. *et al.* Germinal center dynamics revealed by multiphoton microscopy with a photoactivatable fluorescent reporter. *Cell* **143,** 592–605 (2010).
18. Gitlin, A. D., Shulman, Z. & Nussenzweig, M. C. Clonal selection in the germinal centre by regulated proliferation and hypermutation. *Nature* **509,** 637–640 (2014).
19. Basso, K. *et al.* Tracking CD40 signaling during germinal center development. *Blood* **104,** 4088–4096 (2004).
20. Heise, N. *et al.* Germinal center B cell maintenance and differentiation are controlled by distinct NF-κB transcription factor subunits. *J. Exp. Med.* **211,** 2103–2118 (2014).
21. Mueller, J., Matloubian, M. & Zikherman, J. Cutting edge: An in vivo reporter reveals active B cell receptor signaling in the germinal center. *J. Immunol.* **194,** 2993–2997 (2015).
22. Basso, K. *et al.* Integrated biochemical and computational approach identifies BCL6 direct target genes controlling multiple pathways in normal germinal center B cells. *Blood* **115,** 975–984 (2010).
23. Khalil, A. M., Cambier, J. C. & Shlomchik, M. J. B cell receptor signal transduction in the GC is short-circuited by high phosphatase activity. *Science* **336,** 1178–1181 (2012).
24. Su, T. T. *et al.* PKC-β controls IκB kinase lipid raft recruitment and activation in response to BCR signaling. *Nat. Immunol.* **3,** 780–786 (2002).
25. Woodside, M. T. *et al.* Nanomechanical measurements of the sequence-dependent folding landscapes of single nucleic acid hairpins. *Proc. Natl. Acad. Sci. USA* **103,** 6190–6195 (2006).
26. Tolar, P. & Spillane, K. M. Force generation in B-cell synapses: mechanisms coupling B-cell receptor binding to antigen internalization and affinity discrimination. *Adv. Immunol.* **123,** 69–100 (2014).
27. Tolar, P., Hanna, J., Krueger, P. D. & Pierce, S. K. The constant region of the membrane immunoglobulin mediates B cell-receptor clustering and signaling in response to membrane antigens. *Immunity* **30,** 44–55 (2009).

28. Seeley-Fallen, M. K. *et al.* Actin-binding protein 1 links B-cell antigen receptors to negative signaling pathways. *Proc. Natl. Acad. Sci. USA* **111,** 9881–9886 (2014).
29. Liu, C. *et al.* N-WASP Is Essential for the Negative Regulation of B Cell Receptor Signaling. *PLoS Biol* **11,** e1001704 (2013).
30. Becker-Herman, S. *et al.* WASp-deficient B cells play a critical, cell-intrinsic role in triggering autoimmunity. *J. Exp. Med.* **208,** 2033–2042 (2011).
31. Brossard, C. *et al.* Multifocal structure of the T cell - dendritic cell synapse. *Eur. J. Immunol.* **35,** 1741–1753 (2005).
32. Hailman, E., Burack, W. R., Shaw, A. S., Dustin, M. L. & Allen, P. M. Immature CD4(+)CD8(+) thymocytes form a multifocal immunological synapse with sustained tyrosine phosphorylation. *Immunity* **16,** 839–848 (2002).
33. Meyer-Hermann, M. *et al.* A theory of germinal center B cell selection, division, and exit. *Cell. Rep.* **2,** 162–174 (2012).
34. Wan, Z. *et al.* B cell activation is regulated by the stiffness properties of the substrate presenting the antigens. *J. Immunol.* **190,** 4661–4675 (2013).
35. Calado, D. P. *et al.* The cell-cycle regulator c-Myc is essential for the formation and maintenance of germinal centers. *Nat. Immunol.* **13,** 1092–1100 (2012).
36. MacLennan, I. C. Germinal centers. *Annu. Rev. Immunol.* **12,** 117–139 (1994).
37. Wang, X. & Ha, T. Defining Single Molecular Forces Required to Activate Integrin and Notch Signaling. *Science* **340,** 991–994 (2013).
38. Zhang, Y., Ge, C., Zhu, C. & Salaita, K. DNA-based digital tension probes reveal integrin forces during early cell adhesion. *Nat. Commun.* **5,** 5167 (2014).
39. Blakely, B. L. *et al.* A DNA-based molecular probe for optically reporting cellular traction forces. *Nat. Methods* **11,** 1229–1232 (2014).
40. Toellner, K.-M. *et al.* Low-level Hypermutation in T Cell-independent Germinal Centers Compared with High Mutation Rates Associated with T Cell-dependent Germinal Centers. *J. Exp. Med.* **195,** 383 (2002).

Figure Legends

Figure 1 Large-scale imaging shows subset-specific differences in B cell synapses. Gating in image datasets on B cell subsets using fluorescence intensities of membrane markers and image galleries of B cell synapses after 20 min incubation with antigen (anti-Igκ) on PLBs. (**a**) Gates show T1 (IgM^+ $CD23^-$) and T2-3 ($IgM^{+/int}$ $CD23^+$) cells. (**b**) Gates show marginal zone (MZ) ($CD21^+$ $CD23^-$) and follicular (FO) ($CD21^{lo}$ $CD23^+$) cells. (**c**) Quantification of synaptic features. Data are means and s.e.m. from n = 92 T1, 161 T2-3, 4504 FO, and 459 MZ cells from one out of three experiments. Scale bar, 5 μm.

Figure 2 GC B cells exhibit unique synaptic architecture. (**a**) Plot of antigen (anti-Igκ) centralization in synapses of B220-positive splenic cells from immunized mice after 20 min on PLBs. Cells with low centralization (red rectangle) are shown in a Fas versus CD38 versus dotplot. (**b**) Galleries showing synapses of Fas^+ $CD38^-$ GC B cells and Fas^- $CD38^+$ follicular naive B cells. (**c**) Quantification of synaptic features of naive and GC B cells. (**d**) Left, galleries of synapses of pre-enriched GC and naive B cells showing F-actin localization in the synapse plane. Right, correlation of actin and antigen fluorescence in the synapse. (**e**) Antigen centralization and maximum projection images of synapses of naive ($B220^+$ Fas^- $CD38^+$ IgM^+ $IgG1^-$), pre-enriched GC B cells ($B220^+$ Fas^+ $CD38^-$ IgM^+ $IgG1^-$ or $B220^+$ Fas^+ $CD38^-$ IgM^- $IgG1^+$, and IgG-memory B cells ($B220^+$ Fas^- $CD38^+$ IgM^- $IgG1^+$) imaged on the same PLB. Data are from one experiment representative of two (**d**), three (**a,b,c**) or four (**e**) independent experiments. Means and s.e.m from n = 1596 (**c**), 453 (**d**) naïve and 28 (**c**) or 65 (**d**) GC b cells. **** = $p < 10^{-4}$, ** = $p < 0.005$ in unpaired t-tests. Scale bars, 5 μm.

Figure 3 Live cell imaging reveals the dynamics of synapse formation in naive and GC B cells. (**a**) Kymographs of antigen (anti-Igκ) in the synapses on PLBs. (**b**) Fluorescence intensities of antigen clusters tracked from their appearance to fusion with other clusters or their disappearance. (**c**) Growth rates of antigen clusters in the first two minutes of synapse formation. Data are from one cell each from one out of three experiments (**a,b**), or means and s.e.m. of n = 29 naive and 24 GC cell antigen clusters from three experiments (**c**). **** = $p < 10^{-4}$ in an unpaired t-test. Scale bar, 5 μm.

Figure 4 Signaling in naive and GC B cell synapses with PMSs. (**a**) Dot plot of mean synaptic antigen and phospho-BLNK intensities in each cell. Gating shows cells outside (synaptic antigen intensity^{lo}) and on PMSs. (**b**) Images of phospho-BLNK and antigen (anti-Igκ) in the plane of the synapse and in a sideview reconstruction. (**c**) Quantification of intracellular signaling in naive and GC B cells. (-), cells outside of PMSs, +, cells on PMSs. Synapses were analysed after 10 min (p-Syk) or 20 min (all other staining). Data are normalized to the signal in naive cells outside of PMSs. (**d**) Intracellular calcium levels in cells interacting with antigen on PLBs. Left, individual live cell traces of Fluo-4/Fura-Red ratios from one experiment. Right, calcium area under the curve (AUC). Error bars represent mean and s.e.m from n = 3 experiments. * = $p < 0.05$ between GC cells and the corresponding naive cell groups in paired t-tests. Scale bars, 5 μm.

Figure 5 Different activities of PKCs and NFκB, in naive and GC B cells. (**a-f**) Quantification of staining with antibodies against phospho-PKCαβ (**a-c**) and PKCδ (**d-f**). (**a, d**) Levels of synaptic staining analyzed as in Fig. 4. (**b, e**) Recruitment of PKCs to the synapse calculated as the ratio of synaptic to total cell intensity. Data are from the same experiments as in (**a, d**). (**c, f**) Membrane recruitment of PKCs in cells stimulated with PMA plus ionomycin (+) compared to unstimulated cells (-). (**g**) Nuclear translocation of p50. Top, representative images of p50 and DAPI staining in naive and GC B cells unstimulated, or stimulated with glass-attached antigen or CD40L. Bottom, large-scale image quantification of p50 nuclear to cytoplasm ratios. All data are means and s.e.m. from n = 3 (**a-c, f-g**) or 4 (**d, e**) experiments. * = $p < 0.05$ in paired t-tests between the GC and corresponding naive cell groups or between the bracketed groups. Scale bar, 5 μm.

Figure 6 Antigen internalization by naive and GC B cells from synapses with PMSs. (**a**) Quantification of total extracted antigen per cell after 20 min on PMSs. For visualization, cells with zero antigen extraction were assigned a random background value. The box shows cells that interacted with PMSs and therefore were considered for analysis. FU, fluorescence units. (**b**) Features of extracted antigen clusters. (**c**) Sideview sections through the middle of cells showing degradation of a DNA sensor attached to antigen. (**d**) Percent of extracted antigen that was degraded (Deg.) after 30 min on PMSs. Nondeg, antigen labeled with a nondegradable sensor. (**e**) Sideview sections through the middle of cells showing surface staining for antigen. (**f**) Percent of extracted antigen that was internalized after 30 min. (**g**) Effect of inhibition of signaling and myosin contractility on antigen extraction. Data are

means and s.e.m of n = 982 naïve, 854 GC cells from one out of five experiments (**b**), n = 465-982 cells from two experiments (**d,f**). Data in (**g**) show means and s.e.m. normalized to internalization in DMSO-treated naive B cells, n = 3 experiments. **** = $p < 10^{-4}$, *** = $p < 10^{-3}$, * = $p < 0.05$ where p is significance in nonparametric tests (**b, d, f**) or paired t-tests (**g**). Scale bars, 5 μm.

Figure 7 Regulation of antigen binding by mechanical forces in naive and GC B cell synapses. (**a**) Images of sensor fluorescence and the fluorescence ratio indicating 9 pN sensor opening in synapses with PLBs. (**b**) 9 pN force sensor fluorescence and ratios in a tracked BCR-antigen cluster. (**c**) Sensor opening ratios as a function of the sensor opening force. The control sensor lacks the force-sensitive hairpin. (**d**) Mean antigen (anti-Igκ) fluorescence in synapses of cells with or without blebbistatin treatment, normalized by antigen fluorescence outside of cells. Data are means and s.e.m from n = 33-49 (**b**), n = 12-19 (**d**) naive, and 16-59 (**b**), 11-12 (**d**) GC synapses from two (**b**) or three (**d**) experiments. **** $p < 10^{-4}$ in unpaired t-tests. Scale bar, 5 μm.

Figure 8 Affinity discrimination by naive and GC B cells. Naive, CTV-labeled B1-8 B cells were imaged on NP_{15}- or NIP_{15}-containing PMSs together with donor-enriched B cells from mice that received B1-8 B cells and were immunized with SRBC-NIP. (**a**) Levels of phospho-BLNK and (**b**) antigen extraction by B1-8 naive (CTV^+, Fas^-) and GC (CTV^-, Fas^+) B cells. (**c**) Ratio of NIP_{15} to NP_{15} antigen extracted from PMSs by the B1-8 naive and GC B cells. Data show mean and s.e.m. normalized to values of naive B cells on NIP_{15} from n = 1693 and 1517 naive, and 81 and 84 GC B cells aggregated from five experiments **(a, b**), or mean and s.e.m from n = 5 experiments (**c**). **** = $p < 10^{-4}$ in nonparametric tests (**b**) or in a paired t-test (**c**).

Methods

Mice, immunizations and cell transfers.

C57BL/6 mice were used as the source of naive B cells unless otherwise stated. B1-8$^{flox/flox}$ Igκ-$^{Ctm1Cgn/tm1Cgn}$mice on C57BL/6 background (B1-8 mice) were used as a source of B1-8 B cells specific for the NP and NIP haptens. All mice were between 1-6 months old and were male and female. Mice were bred and treated in accordance with guidelines set by the UK Home Office and the Francis Crick Institute Ethical Review Panel.

To generate GC B cells, C57BL/6 mice were immunized with SRBCs (Patricell). SRBCs were stored in sterile Alsever's solution at 4 °C and washed three times in phosphate buffered saline solution (PBS) before intra-peritoneal injection of 10% v/v SRBC solution in 200 μl PBS. SRBC-immunized mice were used at day 7–14. For GC B cell imaging, splenocytes were pooled from two mice per experiment.

Antigen-specific GC B cells were generated by adoptive transfer of 5×10^6 splenocytes from B1-8 mice (expressing CD45.2) in 0.1 ml Iscove's Modified Dulbecco's Medium into congenic C57BL/6 CD45.1 or (C57BL/6 × C57BL/6 CD45.1) F1 mice via tail vein injection. Immediately after cell transfer the mice were immunized with SRBCs conjugated with NIP. The conjugation was performed by incubating SRBCs with NIP-e-Aminocaproyl-OSu (Biosearch Technologies) in 0.15 M $NaHCO_3$, pH 8.3, for 2 h. Conjugated SRBCs were washed three times in PBS and resuspended at 10% v/v in PBS before injection. The conjugation was confirmed by staining the SRBCs with Cy5-labeled recombinant B1-8 Fab fragment[10] and measuring with flow cytometry. Mice immunized with SRBC-NIP were used at day 6–10 post immunization. Splenocytes were pooled from three mice per experiment.

Antibodies and reagents for large-scale imaging

Antibodies for cell enrichment, flow cytometry and large-scale imaging are described in **Supplementary Table 1**. The goat $F(ab')_2$ anti-mouse Igκ (Southern Biotech) that was used as antigen was biotinylated with NHS-LC-LC-biotin (Pierce) and labelled with Cy3 or Cy5 (GE Healthcare). NP_{15} and NIP_{15} antigens were prepared by biotinylating and Cy5 labeling a goat IgG $F(ab')_2$ fragment (Jackson Immunoresarch) followed by haptenation with 4-hydroxy-3-nitrophenylacetic acid active ester (NP-OSu) or 4-hydroxy-3-iodo-5-nitrophenylacetic active ester (NIP-OSu; Biosearch Technologies) and removal of free haptens on Zeba desalting columns (Pierce).

Cells, cell isolation and enrichment.

HEK293 cells were grown in suspension at 37 °C in Pro-293 medium (Lonza) supplemented with 1.5% fetal bovine serum (Biosera) and 2 mM l-glutamine (PAA Laboratories). Primary splenocytes were obtained from the spleen by passing through a 70 μm cell strainer and lysing red blood cells using ACK buffer (Gibco). Naive B cells were isolated by negative selection using anti-CD43 microbeads (Miltenyi Biotech). GC B cells were enriched from splenocytes of immunized mice by negative selection using biotinylated anti-CD43, anti-IgD and anti-CD11c antibodies and anti-biotin microbeads (Miltenyi Biotech). For the enrichment of transferred B1-8 B cells, the negative selection was supplemented with biotinylated anti-CD45.1, which is expressed by the host cells. After enrichment, cells were recovered in RPMI 1640 media (Sigma) supplemented with 10% fetal bovine serum (Biosera), 1% MEM non-essential amino acids (GIBCO), 2 mM l-glutamine (PAA Laboratories), 50 μM 2-mercaptoethanol (GIBCO), 100 U/ml penicillin and 100 μg/ml streptomycin.

Substrates for imaging of synapses.

PLBs were prepared by fusing small unilamellar lipid vesicles to clean coverslips as previously described[27]. Briefly, 1,2-dioleoyl-*sn*-glycerol-3-phosphocholine (DOPC) and 1,2-dioleoyl-*sn*-glycero-3-phosphoethanolamine-N-(cap biotinyl) (DOPE-cap-biotin, both from Avanti Polar Lipids) were combined in a 100:1 molar ratio in chloroform, dried to a film with a gentle stream of argon and then further under vacuum for 1 h. The lipid film was resuspended in PBS to 5 mM and bath sonicated for 2 h to produce small unilamellar vesicles, which were clarified by ultracentrifugation and filtering. Glass coverslips (Menzel-Gläser) were cleaned with fresh piranha solution (98% H_2SO_4 and 30% H_2O_2 in a 2:1 ratio), rinsed thoroughly with Milli-Q H_2O, dried with argon and glued to the bottom of Lab-Tek 8-well imaging chambers (Nalgene Nunc). Lipids were added at 0.1 mM in PBS to form PLBs, and excess vesicles were washed away with PBS. PLBs were incubated with 1 μg/ml streptavidin for 20 min, washed with PBS, incubated with biotinylated fluorescent antigens for 20 min and then washed again.

PMSs were prepared as described[10]. Briefly, suspension HEK293A cells were seeded onto poly-l-lysine-coated Lab-Tek imaging chambers and cultured overnight in DMEM supplemented with 10% fetal bovine serum (Biosera), 1% MEM non-essential amino acids (GIBCO), 2 mM l-glutamine (PAA Laboratories), 100 U/ml penicillin and 100 μg/ml streptomycin to 100% confluency. Cells were washed in PBS and sonicated with a probe sonicator at 25°C. The exposed glass surfaces were blocked with 1% BSA and 5% v/v

normal goat serum in PBS for 1 h, and then incubated in HBSS 0.1% BSA with 24 nM biotinylated annexin V biotin (BioVision). After washing, PMS were incubated with 1 μg/ml streptavidin for 20 min, washed, incubated with biotinylated fluorescent antigens for 20 min and washed once more before imaging.

Large-scale imaging.

B cells were washed and resuspended in 50 μl of warm HBSS 0.1% BSA. Cells were added to HBSS 0.1% BSA in pre-warmed imaging chambers with the antigen-loaded substrates and incubated for 20 min at 37 °C to allow B cell synapse formation. For inhibitor studies, the cells were pre incubated with the inhibitors for 15 min at 37 °C in HBSS 0.01% BSA before injecting into the imaging chambers containing the same buffers and inhibitor. The inhibitors and their concentrations were: 20 μM PP2 (Tocris), 10 μM Bosutinib (Axon Medchem), 50 μM BAY61-3606 (Sigma), 10 μM PRT-060318 (Axon Medchem), 50 μM Blebbistatin (Sigma), 20 μM Y27632 (Sigma), 20 μM LY294002 (Cell Signaling), 50 nM GDC-0941 (SYNkinase), 10 μM PD0325901(Sigma). Cells were fixed in 2% paraformaldehyde, blocked using normal mouse serum (Jackson ImmunoResearch) and stained for surface markers using antibodies at a final concentration of 1 μg/ml for 30 min at 25°C. Stained cells were washed and fixed again. For intracellular staining, cells were then permeabilized using the FoxP3 fixation/permeabilization kit (eBioscience) on ice, washed with permeabilization buffer, blocked with 5% v/v normal mouse serum and then incubated with the antibody for intracellular staining. F-actin was stained using fluorescently labeled phalloidin. Cells were fixed again before imaging.

All imaging was performed using a motorized Olympus IX81 microscope with a 100× oil objective (Olympus), controlled through Metamorph software (Molecular Devices). For illumination, the following laser sources were used: 405 nm (Changchun New Industries), 488 nm, 514 nm (both lines from LS300, Dynamic Lasers), and 640 nm (Blue Sky Research). Laser beams were passed through excitation filters and combined into a multispectral single mode optical fibre (Oz Optics) connected to the illumination port of the microscope. Emitted fluorescence was filtered by appropriate emission filters using a filter wheel (Sutter). Automated image acquisition was performed using a motorized stage with an integrated piezo Z-drive (Applied Scientific Instruments). Metamorph journals were used to systematically acquire images from multiple fields of view in each imaging chamber and to move between chambers. Hanging drops of oil on the bottom of the imaging chambers were used to supplement immersion oil during stage movement between chambers. Focus was

maintained using either the ZDC autofocus unit (Olympus), or, in experiments using Cy7 emission, software autofocus using the antigen fluorescence on the substrates.

Large-scale image processing and analysis.

Images were processed and analyzed by a user-guided pipeline implemented in Matlab (Mathworks) tethered to ImageJ by the MIJ plugin (http://bigwww.epfl.ch/sage/soft/mij/). We programmed three interactive modules for (1) determination of background, flatfield and calculation of spectral bleedthroughs, (2) processing 3D multichannel images for identification of cells and their analysis, and (3) display and gating of the data, including generation of image galleries for visual inspection of the results. The code is available upon request.

Background and flatfield images for each channel were obtained from spatially smoothened images of empty imaging wells, or wells with the labelling antibodies adsorbed to coverslips, respectively. We used 2D background and flatfield images for each channel. Channel alignment was pre-determined by imaging multicolor beads. Single color controls for spectral unmixing were obtained using images of fluorophore-labeled antibodies adsorbed to coverslips. Flatfield images were normalized to the mean of their pixel values. All image sets were aligned and cropped to remove poorly illuminated areas at the edges. 2D spectral bleedthrough images were obtained after background subtraction and flatfield correction of the single color images for each channel pair, generating per-pixel bleedthrough correction factors. We found that per-pixel spectral unmixing of experimental samples improved the accuracy of spectral unmixing for 3D multicolor images because of the significant photobleaching of the fluorophores that occurred during sequential acquisition of the channels. All experimental image sets were cropped, aligned, background subtracted and corrected for flatfield and spectral bleedthroughs. Corrected images were saved for visual inspection of identified cells and further analysis.

Cells were detected in the B220 channel using an initial geometric detection in 2D followed by refinement of the cells' edges in 3D. Initially, object edges were detected in mean-projected images using bandpass filtering and Sobel edge detection with user defined parameters. Cell-like objects were identified using circle detection by Hugh transforms with a user-specified radius range. Circles overlapping by more than their radius were merged as one object. After this initial object detection, the images were normalized by smoothened masks of the identified objects to equalize the staining intensity of the membranes of the cells in the image. Scattering of the fluorescence was reduced by dividing the fluorescence images

by their corresponding brightfield images, which contain bright areas around cells. Cell edges were then refined in a 2D maximum projection image by an outward propagation algorithm, in which the cell's edge was identified in 32 radial segments as a distance from the cell's center, where the intensity of the radial segment drops by a user-defined factor compared to the mean intensity of the centripetal pixels of the segment. This algorithm was used iteratively and greatly improved performance over global thresholding for cells with uneven staining along the plasma membrane. The outer edges were limited by regions defined by Voronoi-based segmentation of the image seeded by the centers of the original circles[41]. After identifying the edges of the cells in the maximum projections, the propagation algorithm was repeated in 3D with the 2D objects serving as an outward limit for the propagation. Cells touching the edges of the image were excluded from further analysis. The resulting 3D masks containing cell identification numbers were stored as image stacks. All subsequent analysis of cells was based on these masks.

To exclude incorrectly segmented cells as well as noncellular debris, we developed CellScore - an empirical score of the likelihood that the detected object represents an intact cell. To calculate CellScore for each object, we calculated the mean pixel intensities in five concentric rings normalized by the mean object intensity using channels containing a membrane marker (typically B220) and brightfield (**Supplementary Fig. 1b**). The resulting normalized profiles were correlated with mean profiles obtained from a small number of manually segmented cells. The final CellScore was an average of the correlation coefficients of the profiles in the B220 and the brightfield channels. All image data sets were then gated on intact cells using a dotplot of B220 versus CellScore (**Supplementary Fig. 1c**).

Fluorescence intensity of the cells was calculated as the mean intensity of the pixels identified by the cell masks in each of the channels. The image plane of the antigen-containing substrate (synapse plane) was identified in each image by searching for the plane with the highest mean squared gradient of neighboring pixel values. This focal plane was used to analyze fluorescence intensities and spatial patterns of immune synapses. Synapse size was calculated as the area of the cell mask at the synapse plane. Mean fluorescence in the synapse was the mean intensity of the pixels in the synapse area. Antigen centralization was calculated as the inverse of the intensity-weighted mean of the distances of the pixels from the center of the mass of the synapse, normalized by the mean pixel distance. Synaptic cSMACs were identified from low pass-filtered antigen images as the area of contiguous above-background antigen fluorescence in the center of the synapse. Clusters in the pSMAC

were detected in the antigen channel after bandpass filtering as the local maxima outside of the cSMAC.

Antigen extraction by each cell was analyzed from the *z*-stack images by an improved version of a previously described algorithm[10]. Briefly, each image plane was bandpass-filtered and antigen clusters were identified in planes above the synapse by using a user-specified global threshold. To correct for antigen fluorescence scattered from the substrate, local background was subtracted from each identified cluster using a 3-pixel-wide rim around the cluster in each plane. Other clusters were excluded from the background. Total fluorescence of extracted antigen was calculated as the sum of pixel intensities of the background-corrected extracted clusters. The masks of the extracted antigen clusters were used to calculate the number and mean intensities of the extracted antigen clusters in each cell. Masks containing the extracted antigen clusters were used to quantify fluorescence in other channels. For display in dot plots, cells with zero extracted antigen were assigned a random value derived from the background of the antigen channel.

All data from image and object analysis, including locations of the objects in the images, were stored in an SQLite database. Data were inspected using a custom written set of visualization tools in Matlab for interactive data display in dot plots and histograms, manual gating, generation of image and cell galleries, and export of data for further statistical analysis.

Sideview reconstruction of cells was performed using deconvolution as described[10].

Calcium imaging.

Pre-enriched GC or naive cells were loaded with Fura-Red and Fluo-4 (Invitrogen) at 37 °C in RPMI 5% FCS, washed and transferred into HBSS 0.1% BSA for imaging. Cells were imaged on fluorescently labelled antigen loaded PLBs for 20-30 min by time-lapse 3D acquisition with *z*-stacks acquired every 20 s in the Fluo-4 and Fura-Red channels. TIRF images of the antigen were acquired at the end of each timelapse. Fluo-4/Fura-Red ratios were calculated from the cell body for naive cells and for cells in the GC sample that showed the characteristic GC synapse shape.

PMA and ionomycin stimulation.

Naive and pre-enriched GC B cells were mixed and incubated with 50 ng/ml PMA and 500 ng/ml ionomycin for 10 min at 37 °C, and then allowed to settle onto poly-L-lysine coated imaging chambers for 10 min. Cells were fixed in 2% PFA, stained for surface markers,

permeabilized, blocked and stained for PKCs. Plasma membrane translocation for each cell was calculated as the ratio of the mean fluorescence intensity of a 3-pixel-thick perimeter region to the mean fluorescence intensity of the whole cell.

NF-κB nuclear translocation assay.

Imaging chambers were coated with 2.5 μg/ml anti-Igκ-biotin-Cy5 antigen or 1 μg/ml CD40L (R&D Systems). Naive and pre-enriched GC B cells were mixed in HBSS/0.1% BSA at 37 °C, added to the imaging chambers and incubated for 1 h before fixing in 2% PFA. Cells settled on poly-L-lysine coated chambers for 15 min served as non-activated controls. Wells were blocked with normal mouse serum (Jackson) before surface staining, permeabilization and intracellular staining with anti-NF-κB1 p105/p50. Cells were then incubated with secondary antibody anti-rabbit IgG –Alexa Fluor 488 and with DAPI to stain nuclei. Cells were finally fixed in 2% PFA and imaged. Cells were segmented using the DAPI stain into the nuclear volume and the cytosol using a thresholded DAPI image. The segmentation threshold was determined in each cell as a value three times higher then the background DAPI intensity in the perimeter of the cell. Nuclear translocation of p50 for each cell was calculated as the ratio of the mean fluorescence intensity of p50 staining in the nucleus to the mean intensity in the cytoplasm.

Measurement of antigen degradation, internalization and signaling.

The degradation sensor consists of a double stranded DNA oligonucleotide formed through annealing the fluorescent and quencher single stranded oligomers with the following sequences:

Fluorescent strand sequence: 5′ – Atto647N – TCCGGCTGCCTCGCTGCCGTCGCCA – biotin; quencher strand sequence: 5′ – TGGCGACGGCAGCGAGGCAGCCGGA – Iowa Black RQ.

To monitor degradation of soluble antigen, splenic B cells from SRBC-immunized mice were incubated on ice with 1 μg/ml biotinylated Cy3-labeled anti-Igκ antigen for 20 min, washed, incubated with 1 μg/ml streptavidin for 20 min, washed, incubated with 100 nM of the degradation sensor, and washed again. Cells were warmed to 37 °C for 0–45 min before fixing, staining for surface markers and quantifying sensor fluorescence by flow cytometry. Percentage of degraded antigen was calculated by dividing the ratio of the Atto647N and Cy3 fluorescence in the experimental samples by the ratio of control samples that lacked the quencher strand.

To measure degradation of antigen extracted from PMSs, biotinylated Cy3-labeled anti-Igκ was attached to streptavidin-coated PMSs and then incubated with streptavidin and the degradation sensors. Extracted antigen was considered degraded in pixels where the Atto647N/Cy3 fluorescence was two times higher then the ratio on PMSs outside of cells.

As an additional control, 2′-OMe phosphorothioate-modified oligomers that are resistant to nuclease degradation were used: control fluorescent strand sequence: 5′ – Atto647N – mU*mC* mC*mG*mG* mC*mU*mG* mC*mC*mU* mC*mG*mC* mU*mG*mC* mC*mG*mU* mC*mG*mC* mC*mA – biotin; control quencher strand sequence: 5′ – mU*mC* mC*mG*mG* mC*mU*mG* mC*mC*mU* mC*mG*mC* mU*mG*mC* mC*mG*mU* mC*mG*mC* mC*mA – Iowa Black RQ.

To monitor internalization of soluble antigen, splenocytes from SRBC-immunized mice were incubated on ice with 1 μg/ml biotinylated Cy3-labeled anti-Igκ antigen for 20 min, washed, and incubated for 0–45 min at 37 °C, before fixing and staining with 1 μg/ml Cy5-labeled streptavidin for 20 min. Cells were stained with for surface markers and analyzed by flow cytometry. Internalization was calculated from the loss of the Cy5 signal compared to the zero time point in the naive and GC populations. To measure internalization of anti-Igκ-Cy5 antigen extracted from PMSs, fixed cells were stained with FITC-labeled $F(ab')_2$ anti-goat Ig (Southern Biotech). Extracted antigen was considered internalized in pixels where the FITC/Cy5 ratio was two times lower than the ratio on PMSs outside of cells.

To measure B cell signaling in response to soluble antigens, splenocytes from SRBC-immunized mice were either left unstimulated or incubated with 15 μg/ml anti-Igκ antigen for 15 min, fixed, stained for surface markers before permeabilization and intracellular staining with phospho-specific antibodies. Intracellular staining was analyzed by flow cytometry in gated naive or GC B cells.

Measurement of soluble monovalent NP/NIP binding

To quantify monovalent binding of NP or NIP to B1-8 naive and GC B cells, NP or NIP was coupled to Atto647N in a 1:1 ratio through a double-stranded DNA oligonucleotide, which was formed through annealing single stranded oligomers with the following sequences:

Fluorescent strand: 5′ -Atto647N- TCCGGCTGCCTCGCTGCCGTCGCCA; complementary strand: 5′ – C6 NH_2 - TGGCGACGGCAGCGAGGCAGCCGGA.

To label the DNA with a single hapten, the oligonucleotide was exchanged into 0.1 M sodium carbonate-sodium bicarbonate buffer, pH 9.1, using a Zeba desalting column and

incubated with a 20-fold molar excess of NP-OSu or NIP-OSu for 30 min at 25°C to haptenate the primary amine. Unreacted hapten was removed and the oligonucleotide exchanged into PBS, pH 7.3, using a desalting column. The 1:1 conjugation ratio was verified by UV/Vis spectroscopy.

To measure binding to naive and GC B cells, cells were stained with antibodies for surface markers and incubated with the indicated concentrations of the monovalent antigens for 20 min on ice. Samples were diluted ten times with PBS immediately before analyzing by flow cytometry. Background was subtracted using staining of naive B cells from C57BL/6 mice, or host-derived GC B cells, respectively.

Force sensors and force imaging

The force sensors consist of three DNA oligonucleotides annealed through hybridization to form upper and lower handles connected by a central hairpin (**Supplementary Fig. 7a**). At the base of the hairpin, a red fluorophore-quencher pair (Atto647N and Iowa Black RQ dark quencher) provides a digital readout of hairpin unwinding; and a second fluorophore, Atto550, on the upper handle reports on the position of the sensor and allows clustering-independent ratiometric analysis. The upper handle of the sensor is covalently attached to the protein antigen, and the lower handle of the sensor is tethered to a membrane substrate through a double biotin-streptavidin linker. The $F_{1/2}$ values of the hairpins, the forces at which 50% of the hairpins unfold, were calculated based on the total free energy of the hairpins as described[25] and were approximately 7, 9, and 14 pN. For control measurements, the hairpin sequence was replaced with a single nucleotide, which prevents separation of the Atto647N from the quencher. Opening of this control sensor would require shearing of the DNA by a force of approximately 57 pN. Control experiments using sensors lacking the quencher showed that quenching of the closed state was better than 95%. The DNA sequences were:

7 pN hairpin strand sequence: 5′ – C6 NH_2 -
TCACGACAGGTTCCTTCGCATCGATATTATATATTAATATATAATTTTTTTTTTTTTT
TATATATTAATATATAATAATTTACTCACAAGCAGTGTGTACA – biotin; 9 pN hairpin strand sequence 5′ – C6 NH_2 -
TCACGACAGGTTCCTTCGCATCGATATTATATATTAATATATAATTTTTTATATAT
TAATATATAATAATTTACTCACAAGCAGTGTGTACA – biotin; 14 pN hairpin strand sequence: 5′ – C6 NH_2 -
TCACGACAGGTTCCTTCGCATCGAGAGTCAACGTCTGGATCCTGTTTTCAGGATC

CAGACGTTGACTCATTTACTCACAAGCAGTGTGTACA – biotin; control strand sequence 5′ – C6 NH_2 - TCACGACAGGTTCCTTCGCATCGATATTTACTCACAAGCAGTGTGTACA – biotin; upper handle complementary strand sequence 5′ – Atto647N - TCGATGCGAAGGAACCTGTCGTGA – S-S; lower handle complementary strand sequence 5′ – biotin - TGTACACACTGCTTGTGAGTAAAT – Iowa Black RQ.

To conjugate sensors to antigen, goat $F(ab')_2$ anti-mouse Igκ (Southern Biotech) was purified by anion exchange chromatography (Mono Q, GE Healthcare) using a buffer gradient composed of 25 mM Tris, pH 8.0, and 100-1000 mM NaCl. The protein was exchanged into degassed 1 mM EDTA in PBS, pH 7.3 (PBS-EDTA) using a 7,000 Da molecular weight cutoff desalting column (Zeba, Pierce) and then incubated with a 20-fold molar excess of sulfo-SMCC (Cambridge Biosciences) for 30 min at 25°C. Unreacted sulfo-SMCC was removed with two passes over desalting columns. Equal volumes of 100 μM HPLC purified, single-stranded oligonucleotides (IDT) in 30 mM HEPES, pH 7.5, 100 mM potassium acetate were mixed and annealed in the presence of 2 mM $MgCl_2$. The annealed sensor was exchanged into 0.1 M sodium carbonate-sodium bicarbonate buffer, pH 9.1, using a desalting column and then incubated with a 3-fold molar excess of Atto550 NHS ester for 30 min at 25°C to label the upper-handle primary amine. Excess dye was removed and the sample exchanged into PBS-EDTA using a desalting column. The upper handle dithiol was reduced with 50 mM DTT for 30 min at 25°C and the sensor was passed twice over desalting columns to remove DTT and exchanged into PBS-EDTA. The sensor was mixed with the SMCC-activated antigen in a 1:5 ratio and incubated at 25°C for 2 h. Conjugation was verified by a shift in size on a 2% agarose gel. DNA-protein conjugates were purified by anion exchange chromatography using the same buffer gradient as above.

To measure opening of the force sensors in B cell synapses, imaging chambers were assembled by placing a 10 μl CultureWell gasket (Grace Bio-Labs) onto a piranha-etched glass coverslip attached to a 1-well Lab-Tek chamber. Biotin-containing PLBs were formed in the wells as described above and then loaded with 1 μg/ml streptavidin, washed and loaded with 6 nM force sensor. Naive or enriched GC B cells were added to the wells in 0.1% protease-free BSA in HBSS. Images of the Atto550 and Atto647N fluorescence were acquired using 514 and 640 nm illumination with five second time resolution at 37 °C. The images were aligned, background subtracted and flatfield corrected in ImageJ. Fluorescence in BCR clusters in time-lapse experiments was tracked using previously described

algorithms[27]. For quantification of sensor opening, synapses were analyzed after 20 min of incubation of the cells with the PLBs. Areas around the cell were cropped and the antigen clusters were identified in the Atto550 channel using the threshold function in ImageJ. The ratio of Atto647N to Atto550 fluorescence in each cluster was determined, and the average ratio for each cell was recorded.

Methods-only References:

41. Jones, T. R., Carpenter, A. & Golland, P. Voronoi-based segmentation of cells on image manifolds. *Computer Vision for Biomedical Image Applications* **3765,** 535–543 (2005).

Competing financial interests

The authors declare no competing financial interests.

Figure 1 Large-scale imaging shows subset-specific differences in B cell synapses.

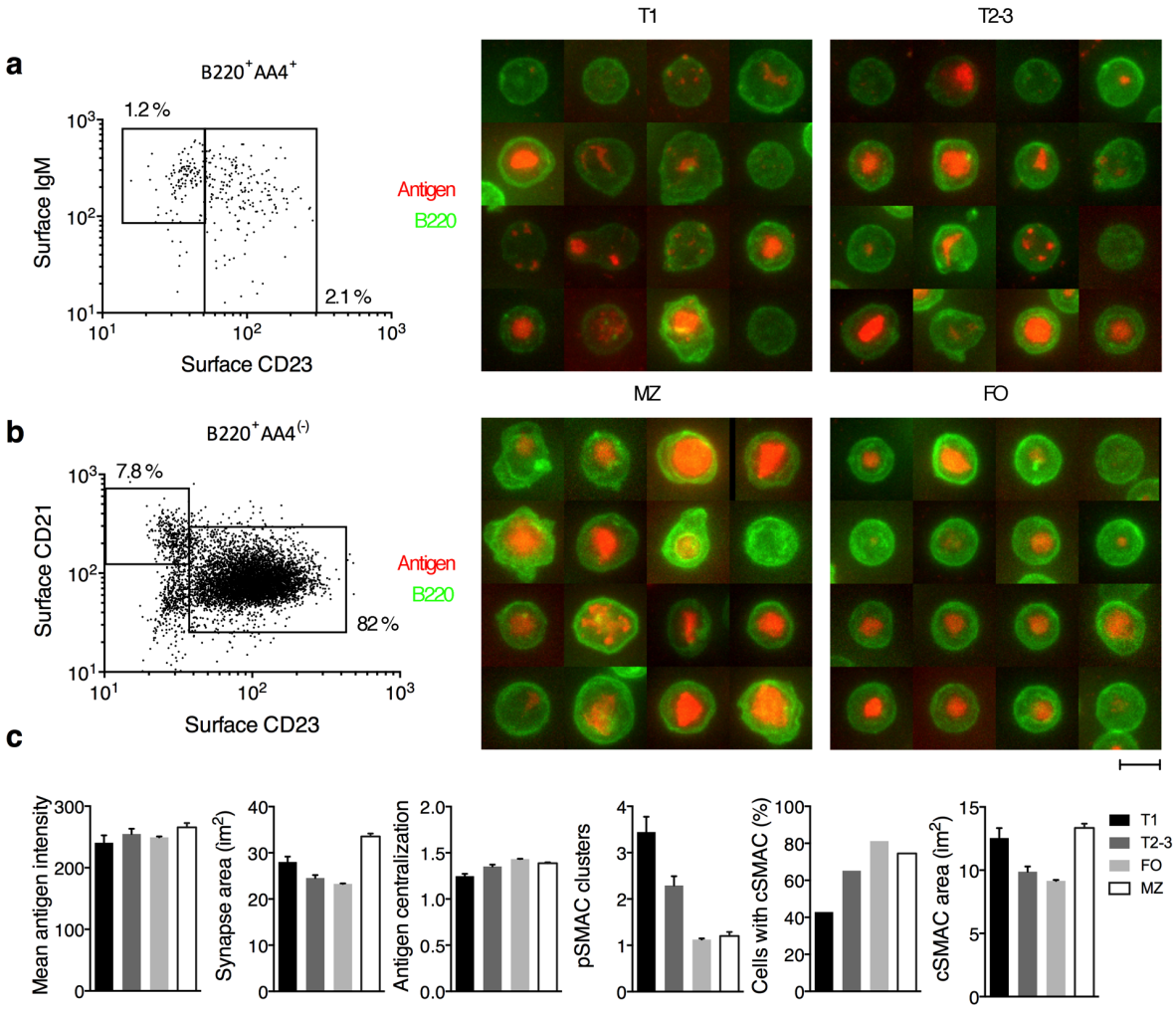


Figure 2 GC B cells exhibit unique synaptic architecture.

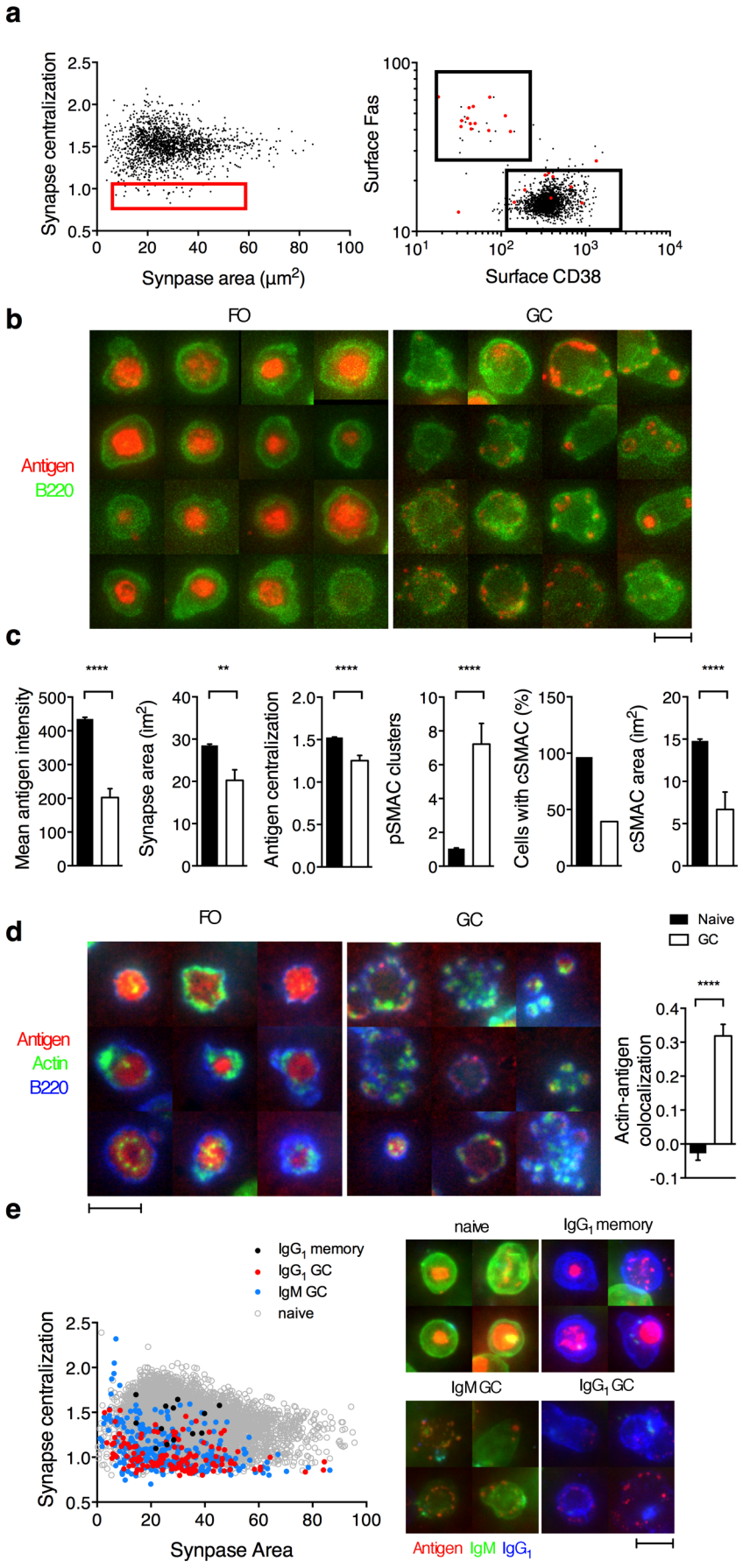


Figure 3 Live cell imaging reveals the dynamics of synapse formation in naive and GC B cells.

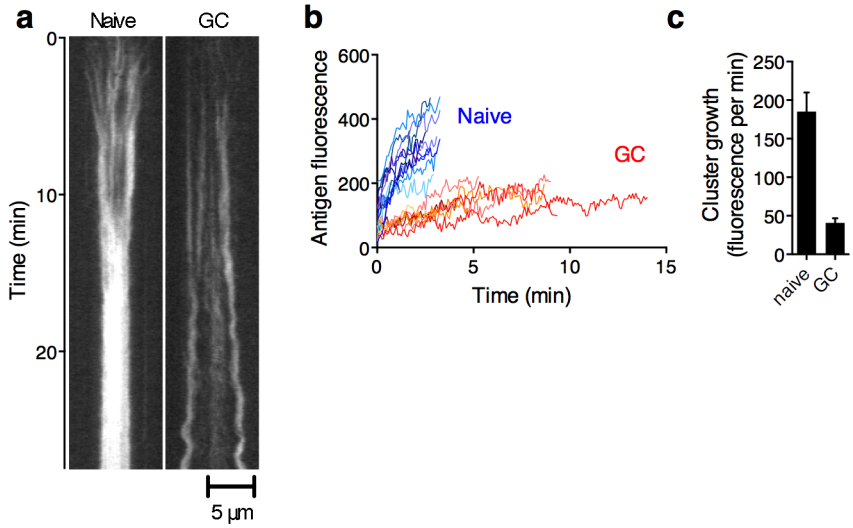


Figure 4 Signaling in naive and GC B cell synapses with PMSs.

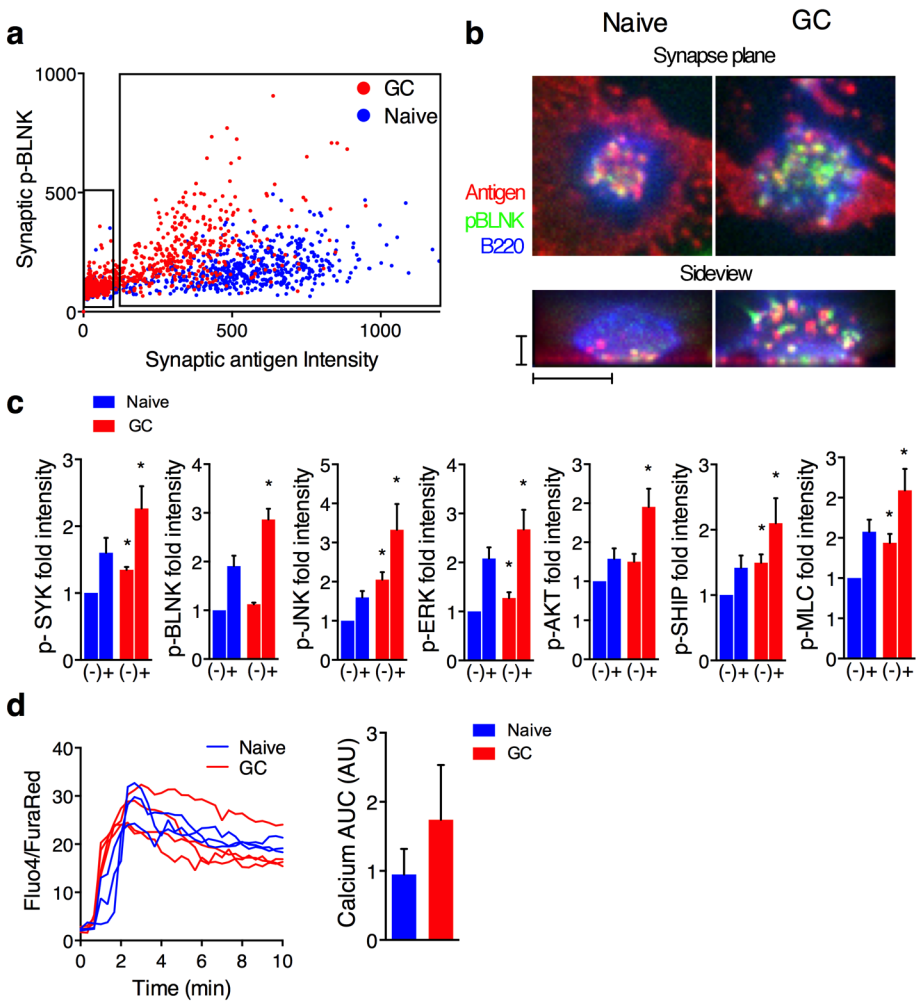


Figure 5 Different activities of PKCs and NFκB, in naive and GC B cells.

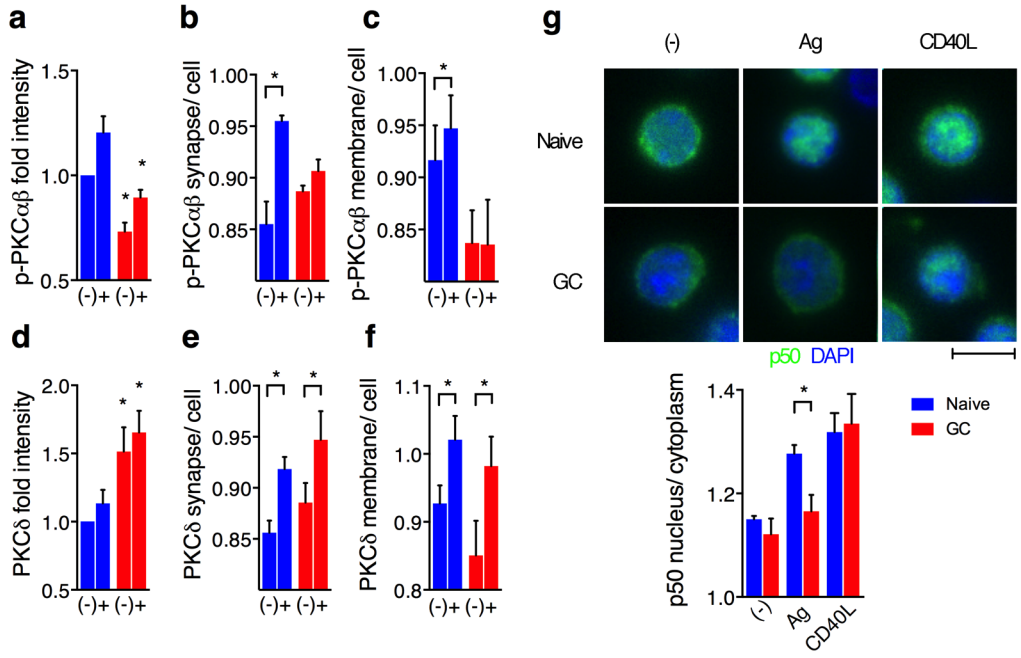


Figure 6 Antigen internalization by naive and GC B cells from synapses with PMSs.

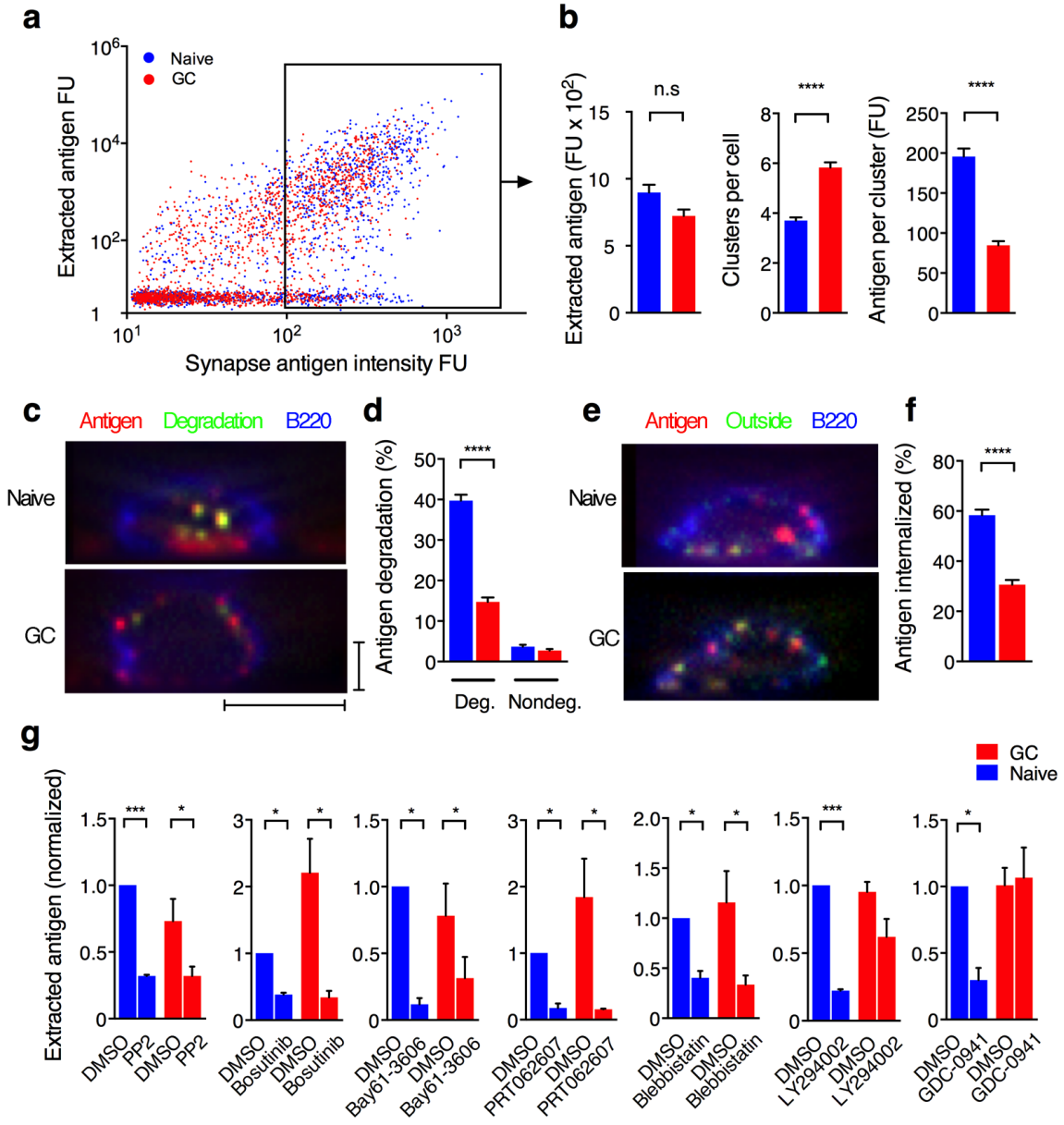


Figure 7 Regulation of antigen binding by mechanical forces in naive and GC B cell synapses.

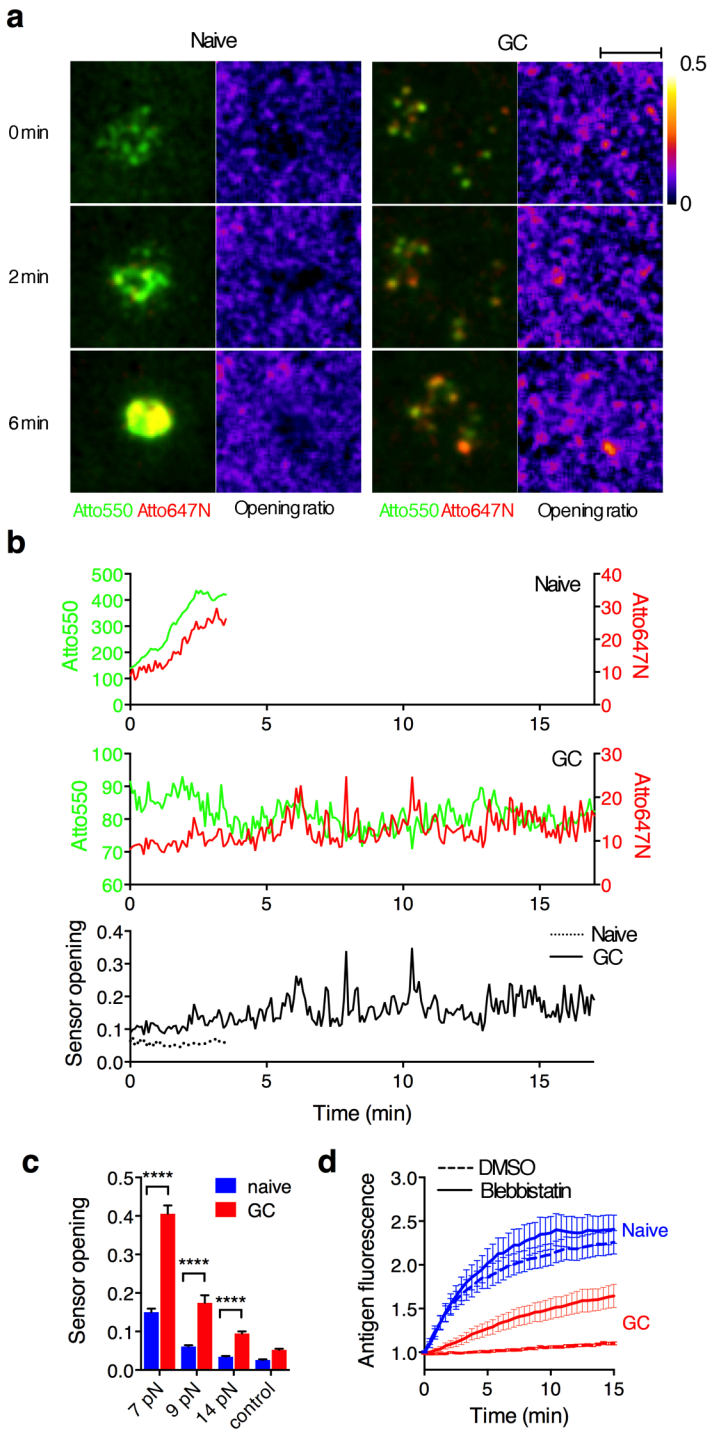
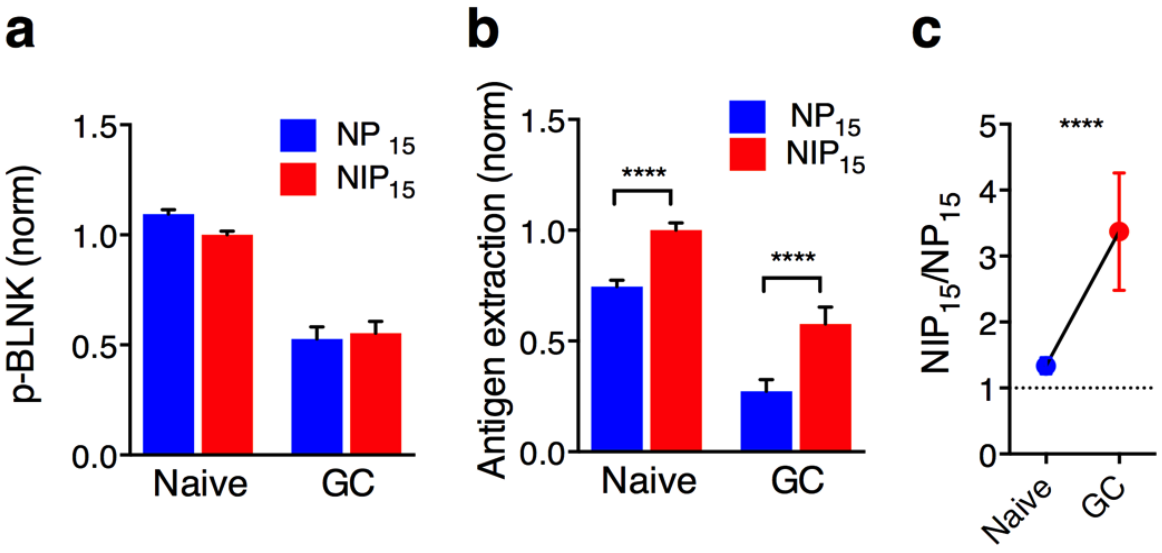
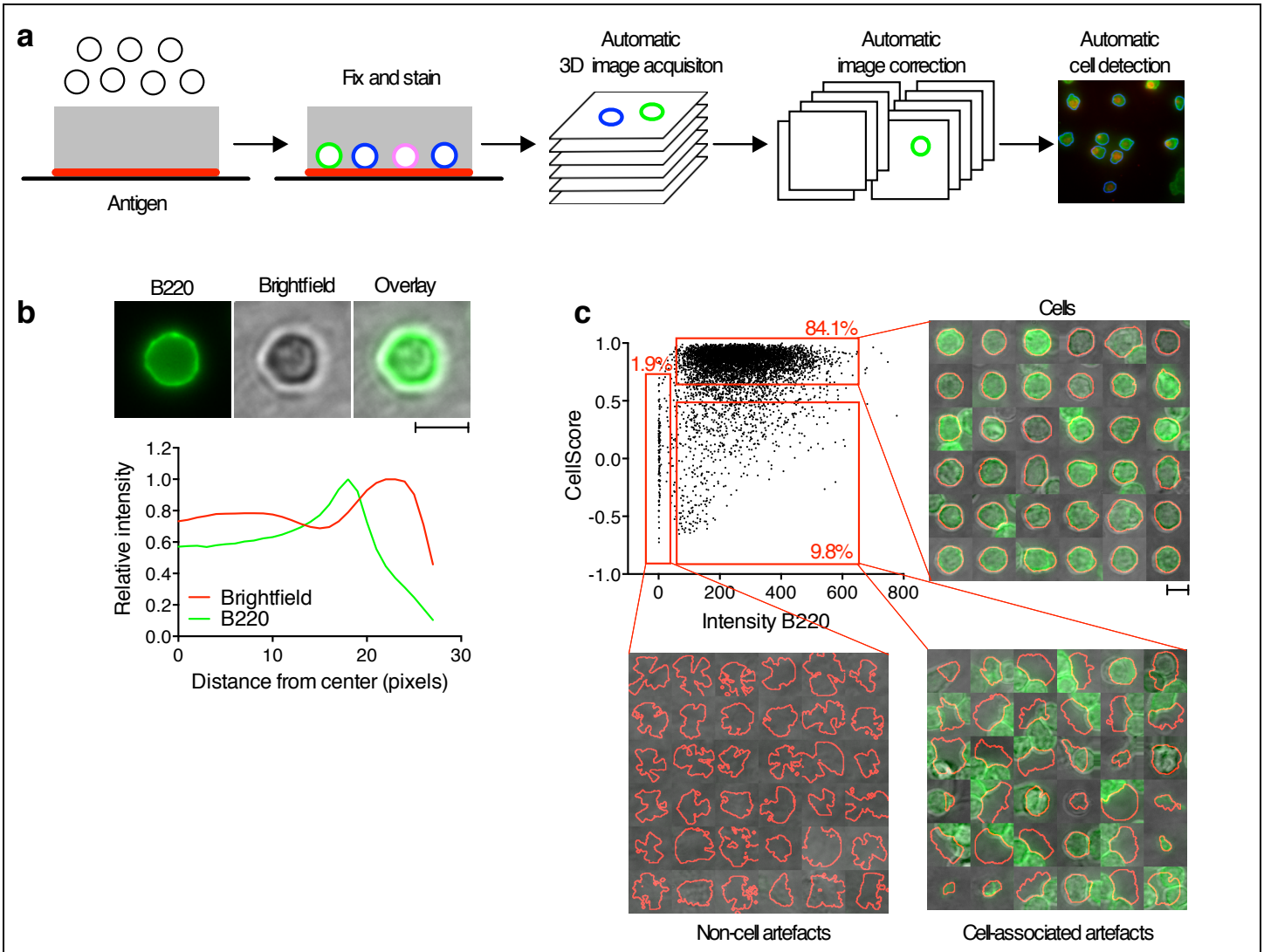


Figure 8 Affinity discrimination by naive and GC B cells.

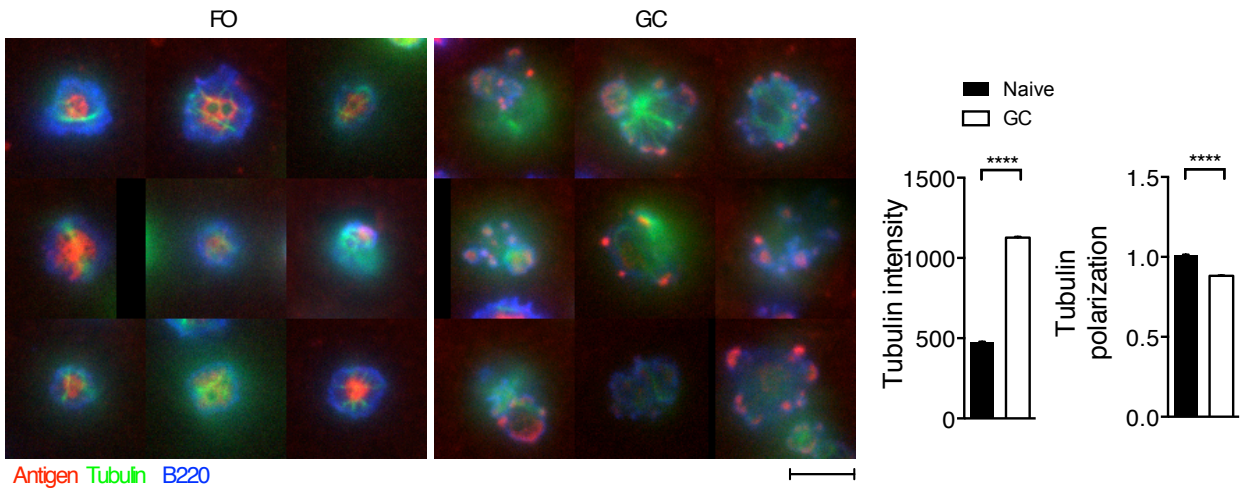




Supplementary Figure 1

Schematic workflow and identifcation of cells in large-scale imaging using CellScore.

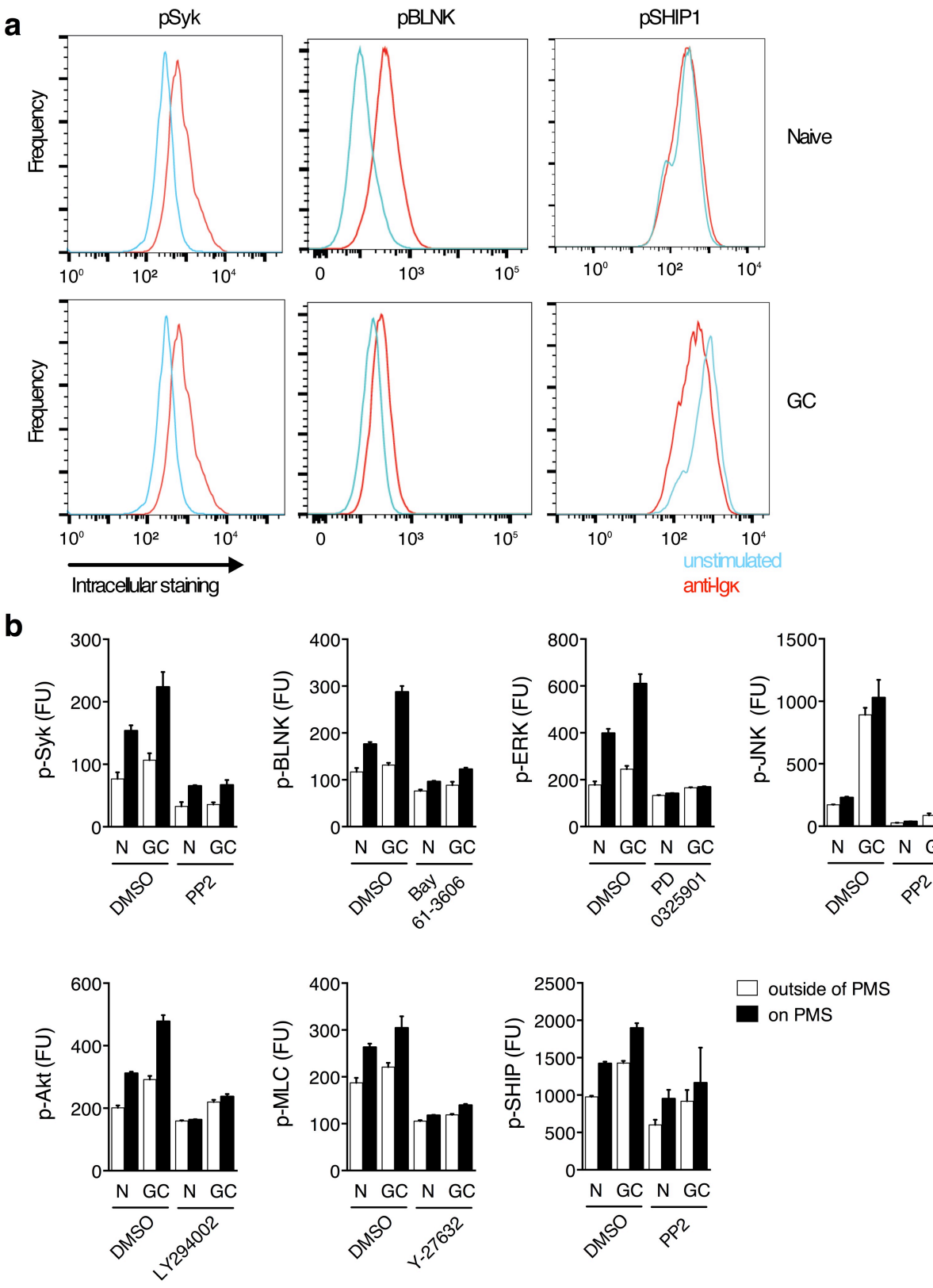
(**a**) Schematic of large-scale imaging workflow, including substrate preparation, loading with B cells, fixing, staining and imaging. (**b**) Mean intensity projection of a cell stained with anti-B220. Plot below shows intensities in the B220 and brightfield channels as mean-normalized radial profiles. Correlation coefficients of the profiles to predetermined ideal profiles of the B220 and brightfield channels are calculated for each object; the average of the two correlations is termed CellScore. (**c**) Plot of CellScore values versus B220 intensity in a typical large-scale experiment. The three gates show correctly identified cells (B220 positive CellScore high), incorrectly identified cells or cell-associated debris (B220-positive, CellScore low), and non-cellular debris and artifacts (B220-negative, CellScore low). Images show B220 staining (green), brightfield (grey) and outlines of the identified objects (red). Scale bars, 5 µm.



Supplementary Figure 2

Reduced polarization of microtubules to immune synapses of GC B cells.

Left, galleries of synaptic planes of naive and GC B cells interacting with antigen (anti-Igκ) on PLBs. Intensity of the tubulin signal was equalized between the two subsets to allow visibility of the individual microtubules in the face of the brighter tubulin staining in GC cells. Right, quantification of overall levels of tubulin staining and of tubulin polarization calculated as the ratio of mean tubulin intensity in the synapse to the mean tubulin intensity in the whole cell. Bar graphs show means and s.e.m. from n = 4429 naive and 3138 GC cells from one out of two experiments. Scale bar, 5 μm.

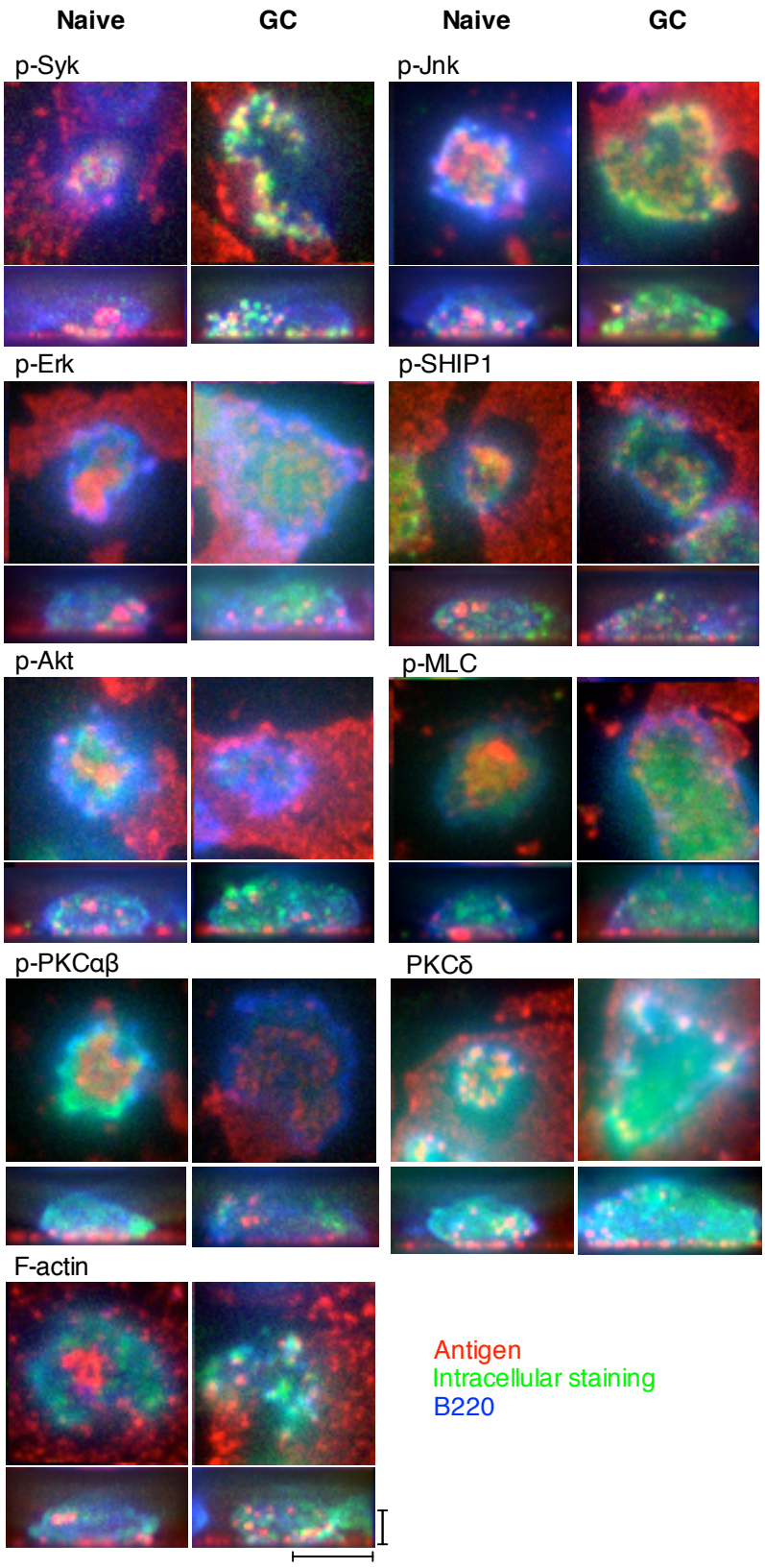


Supplementary Figure 3

Intracellular signaling in naive and GC B cells

(**a**) Intracellular staining in unstimulated and anti-Igκ stimulated naive and GC B cells analyzed by flow cytometry. (**b**) Specificity of phospho-specific intracellular staining in large-scale imaging controlled by inhibitor treatment. Naive and enriched GC B cells were

treated with DMSO or the indicated inhibitors, incubated with PMSs containing anti-Igκ antigen, fixed and stained with the phospho-specific antibodies. Staining was analyzed in synapses (p-Syk, p-BLNK, p-JNK, p-SHIP) or whole cells (p-Erk, p-Akt, p-MLC) gated on naive (N) or GC B cells outside and on the PMSs.

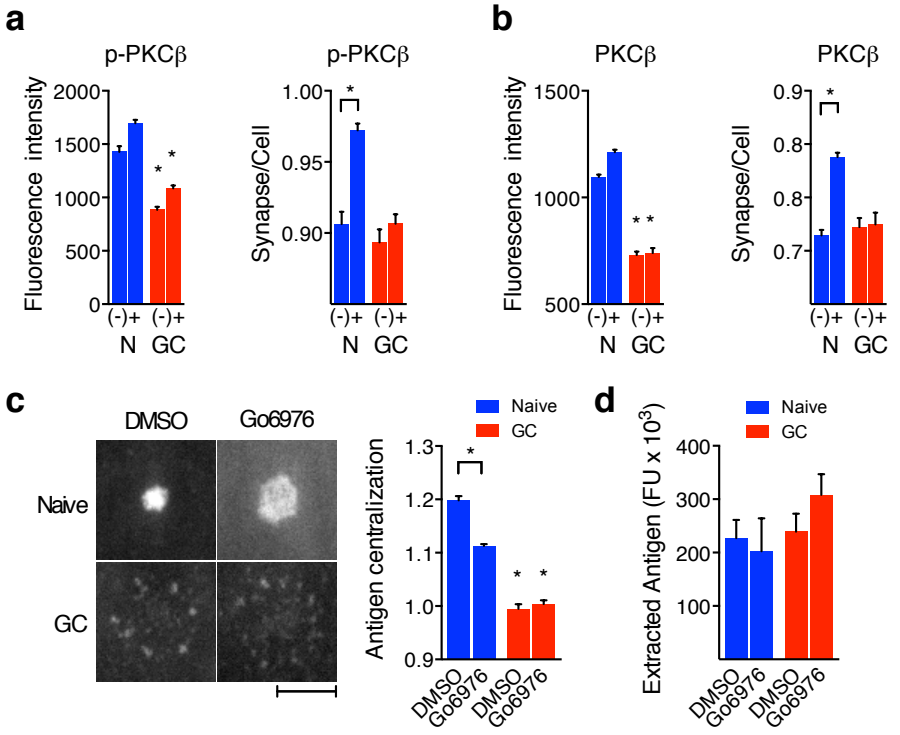


Supplementary Figure 4

Images of intracellular signaling staining

Synapse planes (top panels) and side views (bottom panels) of naive and GC B cells on PMSs showing intracellular staining with the

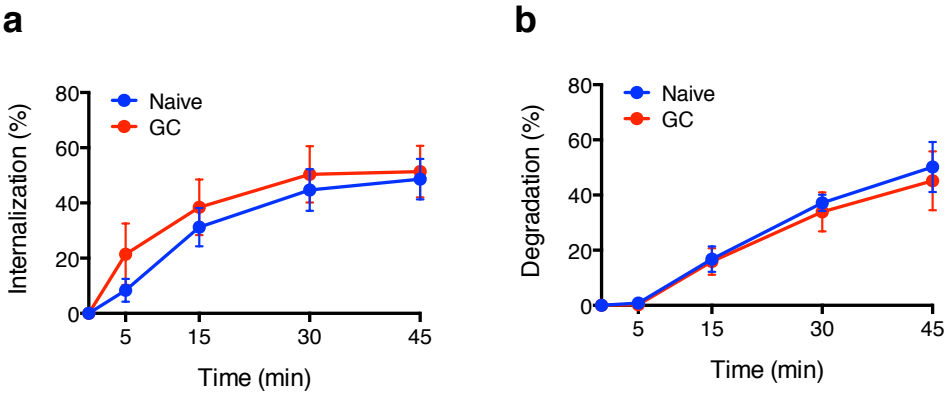
indicated reagents (green). Red, antigen (anti-Igκ), blue, B220 staining. Scalebars, 5 μm.
.



Supplementary Figure 5

Reduced PKCβ activity in GC B cells and consequences of PKCβ inhibition on synaptic architecture and antigen extraction.

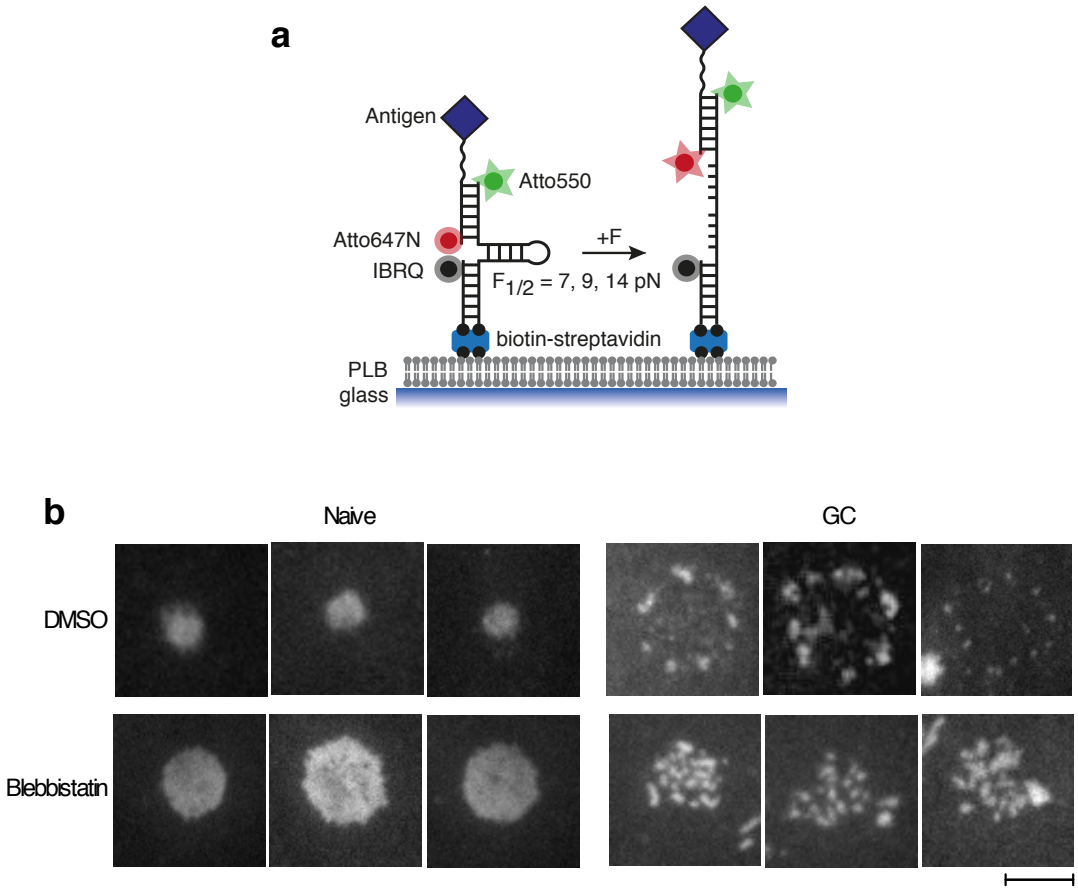
(**a, b**) Quantification of synaptic staining and synaptic recruitment using antibodies recognizing phospho-PKCβ (**a**) and total PKCβ (**b**). Data are from cells recognizing antigen (anti-Igκ) on PMSs and were analyzed as in Fig. 5. (**c**) Representative images of antigen (anti-Igκ) in synapses of naive and GC cells interacting with PLBs and quantification of antigen centralization with or without inhibition of PKCβ with Go6976. (**d**) Quantification of antigen extraction from PMSs with or without inhibition of PKCβ. All bar plots show means and s.e.m. from n = 130-809 naive and 88-184 GC B cells in (**a-c**) and 103-115 naive and 17-27 GC cells in (**d**) representing one out of three experiments. *, p < 10-4 in non-parametric tests between the GC and corresponding naive cells or between the bracketed naive B cell groups. Scale bar, 5 μm.



Supplementary Figure 6

Internalization and degradation of soluble antigen by naive and GC B cells.

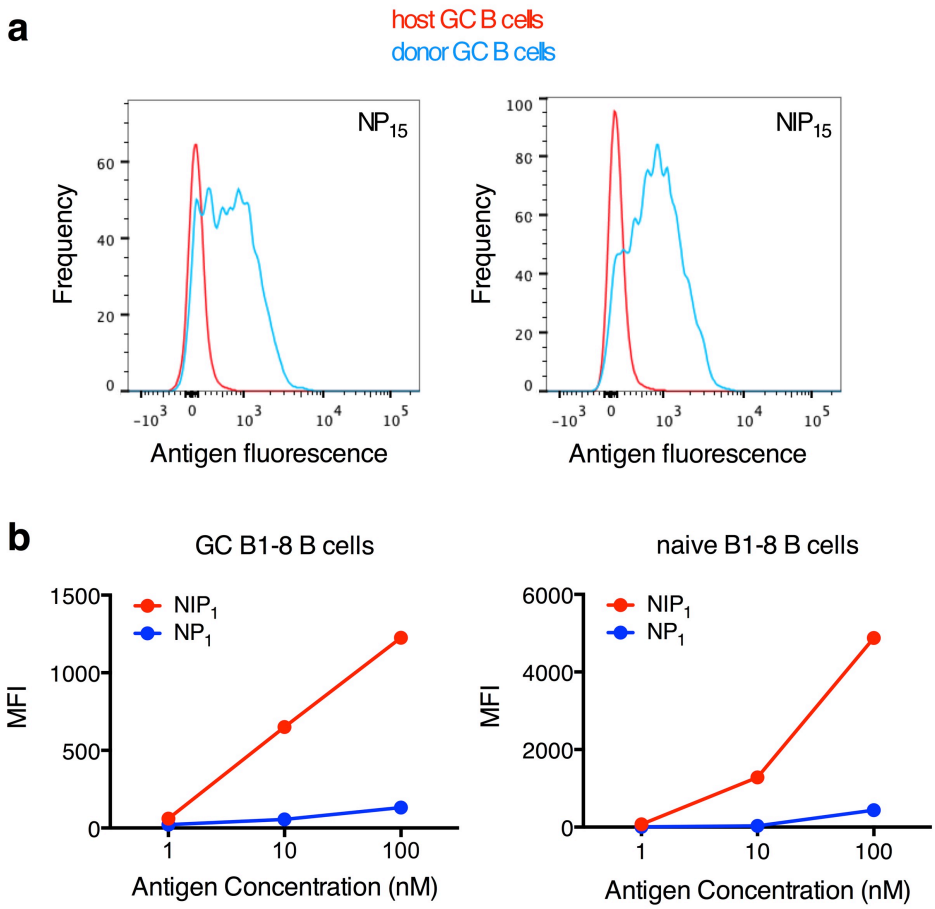
(**a**) Internalization of soluble biotinylated anti-Igκ determined by surface accessibility to streptavidin binding. (**b**) Percentage of degradation of a DNA-based degradation sensor conjugated to anti-Igκ.



Supplementary Figure 7

Force sensor design and synapses of naive and GC B cells interacting with or without inhibition of myosin II by blebbistatin.

(**a**) Schematic explaining the design of sensors used to measure force of BCR pulling. Black 'ladders' depict DNA, with $F_{1/2}$ corresponding to the force required to open the DNA hairpin. The antigen conjugated to the sensor was anti-Igκ. (**b**) Images of antigen (anti-Igκ) in synapses of naïve and GC B cells with or without inhibition of myosin II by blebbistatin. Data are from one out of three experiments analyzed in Fig. 7d. Scale bar, 5 μm.



Supplementary Figure 8

Binding of soluble NP and NIP antigens to naive and GC B1-8 B cells.

(**a**) Staining with NP15 or NIP15 antigens analyzed by flow cytometry in splenic cells of immunized mice that received transferred B1-8 B cells. Staining is analyzed after gating on the transferred B1-8 B cells that differentiated into GC B cells (CD45.2+, Fas+, CD38-) compared to host-derived GC B cells (CD45.1+, Fas+, CD38-). (**b**) Staining of B1-8 naive and GC B cells with monovalent NP and NIP antigens using the indicated concentrations. MFI, mean fluorescence intensity.

Supplementary Movie Legends

Supplementary movie 1. Timelapse imaging of immune synapse formation by naïve and GC B cells. Antigen (anti-Igκ, grey) in naive (left) and GC (right) B cell synapses with PLBs observed using timelapse TIRF microscopy. Time is shown in minutes and seconds.

Supplementary movie 2 Pulling forces in naive and GC B cell synapses observed using timelapse imaging. Synapses with anti-Igκ coupled to a 9 pN force sensor on PLBs in naive (upper panel) and GC (lower panel) B cell synapses. Signals from the force-insensitive label Atto550 (green) and the force-sensitive Atto647N (red) are overlaid on the left panels, and the red-to-green ratio defining opening of the sensor are shown on the right panels. Time is shown in minutes and seconds.